Borehole monitoring of thermo-hydro-mechanical rock slope processes adjacent to an actively retreating glacier

Author(s):
Hugentobler, Marc; Loew, Simon; Aaron, Jordan; Roques, Clément; Oestreicher, Nicolas

Publication date:
2020-08-01

Permanent link:
https://doi.org/10.3929/ethz-b-000412671

Originally published in:
Geomorphology 362, https://doi.org/10.1016/j.geomorph.2020.107190

Funding acknowledgement:
172492 - Paraglacial Rock Slope Mechanics (Phase III) (SNF)

Geomorphology 362 (2020) 107190

Contents lists available at ScienceDirect

Geomorphology

journal homepage: www.elsevier.com/locate/geomorph

Borehole monitoring of thermo-hydro-mechanical rock slope processes adjacent to an actively retreating glacier

Marc Hugentobler *, Simon Loew, Jordan Aaron, Clément Roques, Nicolas Oestreicher

Department of Earth Sciences, Engineering Geology, ETH Zurich, 8092 Zurich, Switzerland

ARTICLE INFO

Article history:
Received 9 January 2020
Received in revised form 30 March 2020
Accepted 31 March 2020
Available online 01 April 2020

Keywords:
Paraglacial rock slope evolution
Thermo-hydro-mechanical coupled effects
Borehole monitoring
Progressive damage
FBG sensors

ABSTRACT

Most natural rock slope failures result from long-term strength degradation. It is often hypothesized that glacial retreat leads to enhanced progressive damage accumulation in adjacent rock slopes, due to mechanical unloading and changes to the thermal and hydraulic boundary conditions. However, direct observations of subsurface processes in a rock slope subject to glacial retreat are rare. In this paper, we present the design, implementation, and performance of a new borehole monitoring system installed on a rock slope in fractured crystalline rock located beside the glacier tongue of the retreating Great Aletsch Glacier (Valais, Switzerland). The three vertical, 50 m deep boreholes were instrumented to continuously monitor groundwater pressure, temperature and deformation at high resolution, in order to investigate thermo-hydro-mechanical coupled slope processes that drive progressive rock mass damage. We show that the system is capable of measuring both reversible and irreversible displacements along single fractures at magnitudes ranging between 0.001 mm to >2 mm in the studied rock slope, and that it is often possible to identify drivers of these deformation signals. The transient subsurface temperature field shows clear indications of former ice occupation in form of cold temperatures preserved at depth and superimposed annual temperature cycles penetrating down to a depth of about 17 m. The variability of the pressure head in the slope is driven by annual snowmelt infiltration cycles, rainfall events, and the assumed connection to englacial water of the temperate glacier. The new and continuously growing dataset presented here will enable us to relate the changing boundary conditions caused by glacial retreat and fatigue from daily to annual thermal and hydraulic loading cycles to progressive rock mass weakening, which may ultimately result in rock slope failure.

1. Introduction

Retreating glaciers induce progressive damage in rock slopes, leading to long-term strength degradation, and ultimately rock slope failure (Augustinus, 1995; Ballantyne, 2002; McColl, 2012). Several hydro- and thermo-mechanical mechanisms have been hypothesized to explain this evolution (Grämiger, 2017; Grämiger et al., 2017, 2018), which are mainly based on geological inference and interpretation of numerical models. To our best knowledge, accurate in-situ monitoring dedicated to the study of subsurface thermo-hydro-mechanical processes driving damage in rock slopes in the context of ice retreat remains absent. Quantification of these thermo-hydro-mechanical coupled processes and their potential to induce damage is critical to understand the long-term evolution of initially stable paraglacial rock slopes that can potentially turn into active slope instabilities. The aim of this paper is to detail the design, implementation and first results of a borehole monitoring system built to quantify damage propagation in rock slopes subject to glacier retreat.

Rock slope failure is often the result of long-term strength degradation (e.g., Gunzburger et al., 2005; Prager et al., 2008; Gischig et al., 2016). The strength of an initially stable slope degrades through time due to stress perturbations caused by different fatigue processes that drive progressive damage. Damage in fractured rock masses occurs through a number of mechanisms, including tensile or shear fracture propagation, breakage of intact rock bridges, degradation of asperities, smoothing of discontinuity surfaces due to shearing, and formation of new fractures (Preisig et al., 2016). Due to the inelastic nature of these damage mechanisms (i.e., deformation remains after stress perturbation), irreversible strain in rock slopes is often used as a proxy to quantify damage (Eberhardt et al., 2004; Gischig et al., 2011b; Preisig et al., 2016; Grämiger et al., 2017; Grämiger et al., 2018). Stress perturbations that cause damage can have several origins, such as thermal stress cycles (i.e., thermo-mechanical fatigue) (Gunzburger et al., 2005; Gischig et al., 2011a, 2011b; Collins and Stock, 2016; Grämiger et al., 2018), water pressure fluctuations (i.e., hydro-mechanical fatigue) (Guglielmi et al., 2005; Preisig et al., 2016; Grämiger, 2017), or dynamic loading from earthquakes (i.e., seismic fatigue) (Gischig et al., 2016). Once a slope is weakened enough, failure can be triggered by a discrete event such as heavy rainfall or an earthquake (e.g., Preisig et al., 2016).

* Corresponding author.
E-mail address: marc.hugentobler@erdw.ethz.ch (M. Hugentobler).

https://doi.org/10.1016/j.geomorph.2020.107190

Several authors have hypothesized that glacial retreat causes changes in thermal and hydraulic boundary conditions, which, in combination with mechanical unloading during glacial retreat, lead to enhanced slope strength degradation (Prager et al., 2008; McColl, 2012; Ballantyne et al., 2014a; Riva et al., 2017; Grämiger et al., 2017, 2018; McColl and Draebing, 2019). Currently, it is assumed that the major processes that cause damage during paraglacial transition in initially stable slopes are stress changes due to: (i) removal of overburden and glacial ice unloading, (ii) short- and long-term subsurface temperature and pore pressure variations caused by the changing glacier boundary condition, and (iii) seismic activity possibly increased by glacio-isostatic adjustment (McColl and Draebing, 2019). The present work focusses on the first two of these processes.

The term "glacial debuttressing", i.e., loss of ice support due to down wasting at the base of a slope, is often hypothesized as a cause for slope failures in the vicinity of retreating glaciers. However, delayed slope response (Prager et al., 2008; Ivy-Ochs et al., 2009; Ballantyne et al., 2014b; Ivy-Ochs et al., 2017) and theoretical considerations (McColl et al., 2010; McColl and Davies, 2013) question the importance of glacial unloading as a major process that propagates damage in adjacent rock slopes. Based on a 2D numerical discontinuum model through the Great Aletsch Glacier Valley, Grämiger et al. (2017) propose that purely mechanical effects of glacial ice loading (and unloading) do not significantly propagate damage and displacement of the adjacent slope, but alter the in-situ stress field, which potentially increases the criticality of fractures.

From numerical investigations, Baroni et al. (2014) and Grämiger et al. (2018) conclude that both long-term (at the time-scale of glacial cycles) and seasonal temperature variations induce significant thermo-mechanical stresses to paraglacial valley flanks, which are able to propagate damage in stable rock slopes. The efficiency of thermo-mechanical forcing of deep rock slope deformation has been shown based on a case study with deformation monitoring data and numerical simulations (Gischig et al., 2011a, 2011b). Gischig et al. (2011a, 2011b) found that thermo-elastic stresses, which are highest near-surface (amplitudes above 1 MPa), extend below the thermally active layer and can drive progressive failure of critically stressed discontinuities to a depth of >100 m. Glaciers impose a strong control on the subglacial temperature regime. Below temperate glaciers, temperatures at the ice-rock interface are kept at a relatively constant value around 0 °C and are shielded from ambient temperature and solar radiation (Wegmann et al., 1998). When glaciers retreat, a new mean annual ground temperature and daily and annual temperature variations alter the subsurface temperature regime and potentially introduce significant thermomechanical stresses (Grämiger et al., 2018).

The amplitudes of annually reversible surface displacements driven by thermo-mechanical stresses are on the order of a few millimeters, while irreversible displacements (fracture slip or opening) depend on slope damage and criticality (Preisig et al., 2016; Grämiger et al., 2017, 2018). In stable crystalline rocks, a single Holocene glacial cycle, such as the Little Ice Age (LIA), might induce cumulative thermo-mechanical slope displacements of a few centimeters (Grämiger et al., 2018). Modeled shear displacements along individual fractures during a glacial cycle (lasting 100 years) are between 1 and 10 mm, i.e., annual irreversible fracture displacements are on the order of 10–100 μm.

Cyclic hydro-mechanical slope processes are known to drive reversible, elastic slope deformation in stable rock slopes (Loew et al., 2007; Hansmann et al., 2012; Rouyet et al., 2017). These mechanisms are also thought to promote progressive slope damage and irreversible displacement (Guglielmi et al., 2008; Prager et al., 2008; McColl, 2012; Ballantyne et al., 2014b; Preisig et al., 2016), and are more efficient than thermo-mechanical loading (Grämiger, 2017). Elastic reversible deformation is normally explained by a pore pressure decrease that causes an increase in effective normal stress on the fracture leading to normal closure, or in the contrary, a pore pressure increase that causes fracture opening (Guglielmi et al., 2008). A comprehensive model for reversible hydro-mechanically coupled rock mass deformations has been presented by Zangerl et al. (2003). Pore pressure increase, and accompanied decrease of effective stress, also causes a reduction of shear strength of the fracture (Rutqvist and Stephansson, 2003; Guglielmi et al., 2008). Thus, if a fracture is critically stressed, a pore pressure increase can promote irreversible slip.

Since temperate glaciers carry large amounts of water, it is often assumed that the phreatic groundwater surface in a glaciated valley flank is tied to the elevation of the phreatic surface within the glacier; so that the temperate glacier has a similar hydraulic head boundary effect on the adjacent slope as a reservoir lake (cf. McColl et al., 2010). In temperate glaciers, subglacial water pressures show a strong seasonal signal, which depends on the subglacial drainage system. During the winter, subglacial water pressures are normally constant, with values of approximately 80% of the ice overburden. Once an efficient subglacial drainage system is established in the summer, the mean subglacial water pressures are lower and daily variations with higher pressures during daytime due to meltwater supply and lower pressures during night occur (Fudge et al., 2005; Harper et al., 2005; Lappegard et al., 2006). High-amplitude diurnal water pressure fluctuations (from atmospheric up to nearly ice overburden pressure) in summer are restricted to regions connected to the main subglacial drainage (Hubbard et al., 1995).

Groundwater table elevations in alpine slopes typically show seasonal variations with higher groundwater levels in spring or early summer due to snowmelt infiltration followed by a long period of recession interrupted by normally smaller events of recharge during rainstorms (de Palézieux and Loew, 2019). The annual amplitude and depth of the phreatic groundwater table are controlled mainly by the ratio of recharge to the hydraulic conductivity of the active layer (Gleeson and Manning, 2008). In fractured crystalline rock, groundwater movement is mainly controlled by fractures and other discontinuities because of the low porosity and permeability of intact crystalline rock (Singhal and Gupta, 2010). Hence, hydraulic conductivity can strongly vary with changing fracture characteristics (i.e., frequency, orientation, aperture, interconnectivity, and persistence, etc.). The recharge response timescales and amplitudes (typically 1–50 m in the Alps) of slope water table variations due to infiltration events are depth-dependent and strongly site-specific (de Palézieux and Loew, 2019).

Hydro-mechanical coupled surface displacements recorded during 5 years by Glueer (2019) in our study area along the Great Aletsch Glacier show both annual reversible magnitudes of about 10 to 20 mm and irreversible magnitudes of about 1 to 2 mm per year. Due to the small irreversible slope displacements, presumably caused by subcritical damage propagation and minor slip along a large number of fractures, and no signs for active slope movement regarding rock mass structure and geomorphology, these slopes will be referred to herein as quasi-stable. Numerical simulations carried out by Grämiger (2017) for these slopes result in irreversible horizontal displacements per glacial hydro-mechanical cycle of about 10 cm and annual hydro-mechanical cycles superimposed on long-term hydro-mechanical effects result in a shear displacement of around 100 μm per year along individual fractures.

Fig. 1 summarizes the above introduced processes and boundary conditions affecting a rock slope adjacent to an actively retreating glacier. The figure illustrates the mechanical, thermal, and hydraulic processes leading to cyclic and permanent stress changes within the rock slope and potentially promotes rock mass fatigue and progressive damage.

In this paper, we present the setup and first data of a new high-resolution borehole-based monitoring system installed in a quasi-stable rock slope adjacent to a deglaciating margin. The unique monitoring system was designed to record multi-annual and daily reversible deformations and irreversible slip along individual fractures (in the ranges described above) and the corresponding main drivers for the

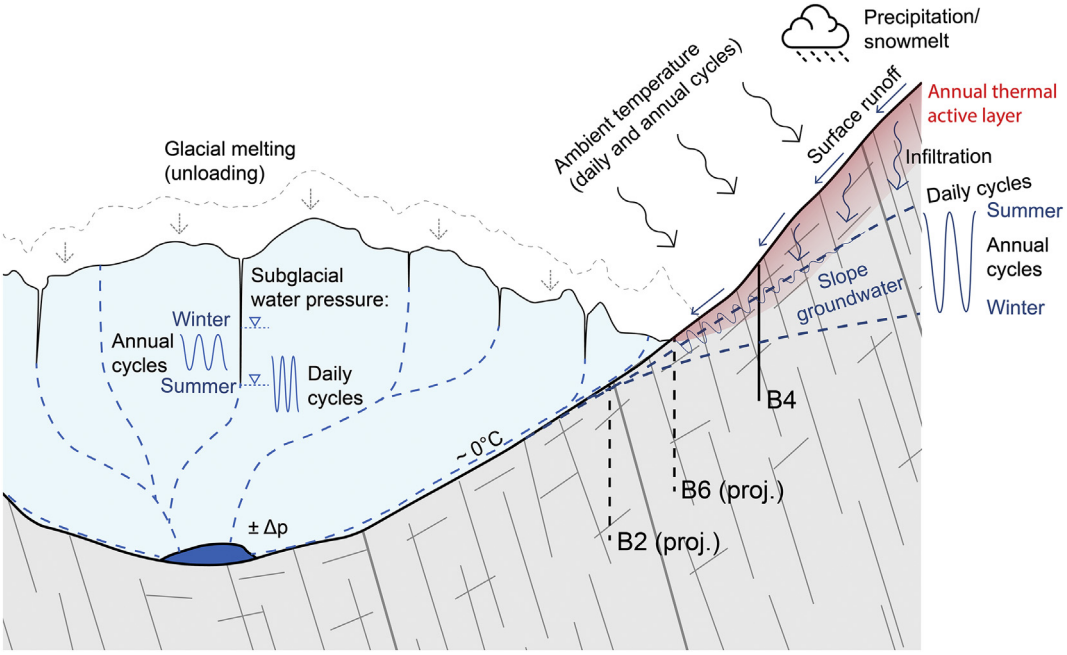

Fig. 1. Illustration of different boundary conditions affecting rock slopes in a deglaciating environment. The schematic cross-section cuts through our central borehole location (B4), and the approximate projected location of B2 and B6 is indicated. The figure is exaggerated by a ratio of 2:1.

deformation. These drivers are the retreat and downwasting of the Great Aletsch Glacier (Switzerland), and fatigue resulting from the annual and daily thermo-mechanical and hydro-mechanical cycles described above. Three vertical, 50 m deep research boreholes (B2, B4, and B6 in Figs. 1, 3) were drilled with short but variable distance from the 2017 lateral ice margin close to the glacier tongue. The research boreholes were logged with geophysical and hydrogeophysical probes to characterize the rock mass structure and its hydrogeological parameters before they were equipped with high-resolution strain (axial and radial), temperature and pore pressure sensors. Additionally, detailed surface structural mapping was conducted in the study area. First, we present a description of the study site and the details of the monitoring system (Sections 2 and 3). Next, we discuss the reliability of the monitoring system, and present data from the first two years of monitoring, to demonstrate the capability and limitations of the system to record thermo-hydro-mechanical coupled reversible displacements and irreversible damage in the glacier adjacent rock slope (Section 4). This is followed by a discussion of the results to date (Section 5). We end with a summary and an outlook (Section 6).

2. Site description

Our research area is situated on a rock slope alongside the retreating glacier tongue of the Great Aletsch Glacier (Figs. 2, 3), Canton Valais, Switzerland. The site can be reached by a one-hour hike along a mountain trail from the Moosfluh cable car station (see Fig. 2). Heavy equipment has to be transported to the site by helicopter. The climatic conditions of the study site are harsh, with many meters of snow between November and May, strong winds, and limited irradiation.

The study site is situated within the Aar-Massif, the largest external crystalline massif of the Central Alps, consisting mainly of granites and gneisses (Steck, 2011) (Fig. 3). The slope is NNW dipping with an average slope angle of about 30°. Bedrock in the area is smoothed by the glacier and has a distinct ridge and furrow morphology. Furrows often follow weak schist layers and brittle-ductile shear zones. A relatively thin recent moraine layer covers parts of the lower study area (Fig. 3).

Borehole televiewer logs in two of the boreholes and surface structural mapping in the study area leads to structure orientations as follows (Fig. 4). The foliation is striking valley subparallel and shows a sub-vertical dip angle, mostly dipping into the slope (i.e., in SE direction). The rock is intersected by three persistent joint sets (F1: Foliation subparallel oriented (mean: 136/85), F2: steeply SSW dipping (mean: 186/86), F3: slope subparallel oriented (mean: 327/31)) and numerous steep, mainly foliation subparallel lying brittle-ductile shear zones. At the surface, joint sets F1 and F3 show a normal spacing of around 1 m and F2 of about 3 m. Borehole televiewer images show a decrease of the fracture density with depth (see Fig. 4). Joint set F2 was not captured with the borehole mapping which could be attributed to a combination of its unfavorable orientation relative to the borehole, its larger normal spacing compared to F1 and F3, and its lower persistence. Field investigation revealed that the brittle-ductile shear zones rarely contain fault gouge, but do feature an increased fracture density and a dense foliation. They are typically a few decimeter wide and show a normal spacing of 10 to 20 m. Glueer et al. (2020) showed that these brittle-ductile shear zones dominate the kinematic behavior of the nearby Moosfluh slope instability (discussed below), and they are expected to also be important for the kinematic behavior of the quasi-stable slopes in our study area. The joint orientations from detailed mapping in our study area agree with the published data from previous studies (Kos et al., 2016; Grämiger et al., 2017; Glueer et al., 2020).

The Great Aletsch Glacier is the largest ice mass in the European Alps and has a current length of about 22 km (GLAMOS, 1881-2018). The Aletsch valley experienced a long history of glacial advances and retreats summarized in Holzhauser et al. (2005). During the Würm glacial period, which presumably lasted ~100 ky and included the last glacial maximum in the Alps (dated at ~30 ky to ~18 ky BP (Ivy-Ochs et al., 2008)), the Aletsch valley was covered by a thick icefield. In the late Pleistocene glacial period, a general ice retreat occurred in the Alps, which was interrupted by a series of readvances (Ivy-Ochs et al., 2008). The maximum extent of the latest of these late Pleistocene readvances, the Egesen stadial (dated at ~12 ky BP) (Kelly et al., 2004; Ivy-Ochs et al., 2008; Schindelwig et al., 2012), is well preserved in moraines and trimlines at the Aletsch valley (Kelly et al., 2004).

The Great Aletsch Glacier strongly retreated during the Holocene interglacial, and showed ice fluctuations at a lower level, with minimum stages comparable to the current ice elevation or lower (e.g., during the Bronze Age Climate Optimum; ~ 3300 years ago (see Fig. 3) and a clear glacial advance at the onset of the Little Ice Age (LIA) with three

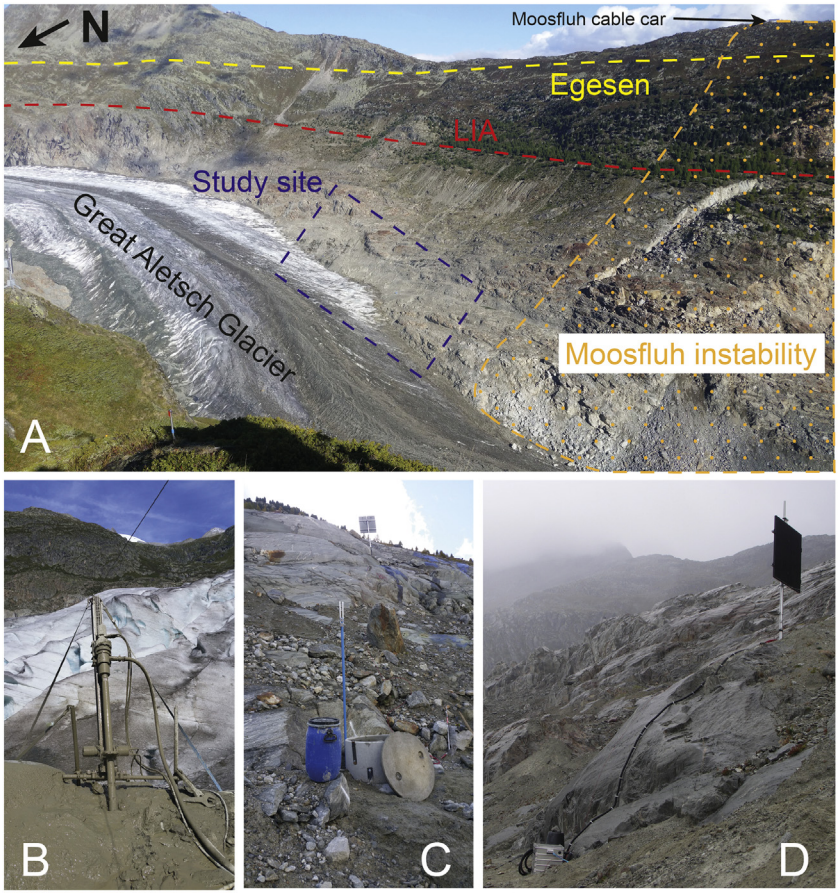

Fig. 2. A) Overview of the study area, showing the Great Aletsch Glacier, the elevation of the approximate LIA and Egesian lateral ice extents, and the location of the Moosfluh slope instability. B) Drilling at B6 location. C) Borehole set-up at B4, notice solar panel in the background. D) Solar panel and control box with batteries and FBG data acquisition system.

local maxima (Holzhauser et al., 2005). The extent of the last LIA ice maxima around 1860 is well preserved by trimlines and lateral moraines in the Aletsch valley (Holzhauser et al., 2005). A comparison of the LIA glacier elevation and the current ice elevation in our study area results in a mean annual vertical ice height loss of 1 to 2 m per year since 1860. However, annually acquired high-resolution digital surface models with a pixel size of 0.5 m provided by the Swiss Federal Office of Topography (swisstopo, JA100120) currently show higher values of about 5–10 m annual ice height loss between 2012 and 2018. The change in ice elevation during this ongoing retreat relative to our borehole locations is illustrated in Fig. 3. The observed ice retreat of the Great Aletsch Glacier is causing the successive exposure of the rock surface in the study area that was ice-covered for probably 2000–3000 years (Holzhauser et al., 2005). The drilling location of B2 has been exposed to the ambient temperature in summer 2017 (i.e., few months before drilling), and glacial ice temporarily returned in winter 2018 for about 4 months (Fig. 3B). The location of B4 was exposed to the ambient temperature in summer 2014 whereas the location of B6 was exposed to ambient temperature in summer 2016 (Fig. 3C, D).

We find a significant number of rock slope instabilities in the area of the current tongue of the Great Aletsch Glacier, including the deep-seated Moosfluh slope instability (Figs. 2, 3). This large toppling-sliding instability was dramatically re-activated in fall 2016, is monitored in detail and has been described and analyzed in several studies (e.g., Strozzi et al., 2010; Kos et al., 2016; Grämiger et al., 2017; Glueer et al., 2019, 2020). Most of the study area including B2 and B4 borehole locations lie in the previously defined quasi-stable rock slopes. The area surrounding borehole B6 has a distinct morphology, including a pronounced headscarp and an outward rotated foliation in the mass below, indicating a toppling rock slope instability (see Fig. 3). Surface and borehole displacement monitoring data currently do not show anomalously high rates of movement here compared to the quasi-stable rock slopes in its surrounding; hence, this rock slope instability is considered to be dormant or relict.

The entire area of the valley around the glacier tongue is monitored with two robotic total stations (or Target Processing System, abbr. TPS), four permanent GNSS stations, several climate stations, two seismic stations, and four time-lapse cameras (for details see Loew et al., 2017; Glueer, 2019).

3. Methods

3.1. Monitoring design and sensor installation

3.1.1. Drilling and logging

The three drilling locations for the research boreholes were chosen at variable distances from the glacier margin and located about 200 to 600 m away from the active Moosfluh slope instability (Fig. 3A). Borehole B2 was drilled directly at the 2017 ice margin, B6 had a lateral distance of about 5 m to the 2017 margin, and B4 was drilled upslope at about 50 m lateral distance to the 2017 ice margin (Fig. 3). The research boreholes (summarized in Table 1) were destructively drilled with a borehole diameter 101 mm by a specialist company that has experience drilling in remote alpine environments. Due to financial and logistical constraints, a light drilling rig was used (see Fig. 2B), which restricted the maximum borehole depth to around 50 m. A total number of six boreholes were initially planned for this study, one vertical borehole and one inclined borehole at each of the three drilling locations. The

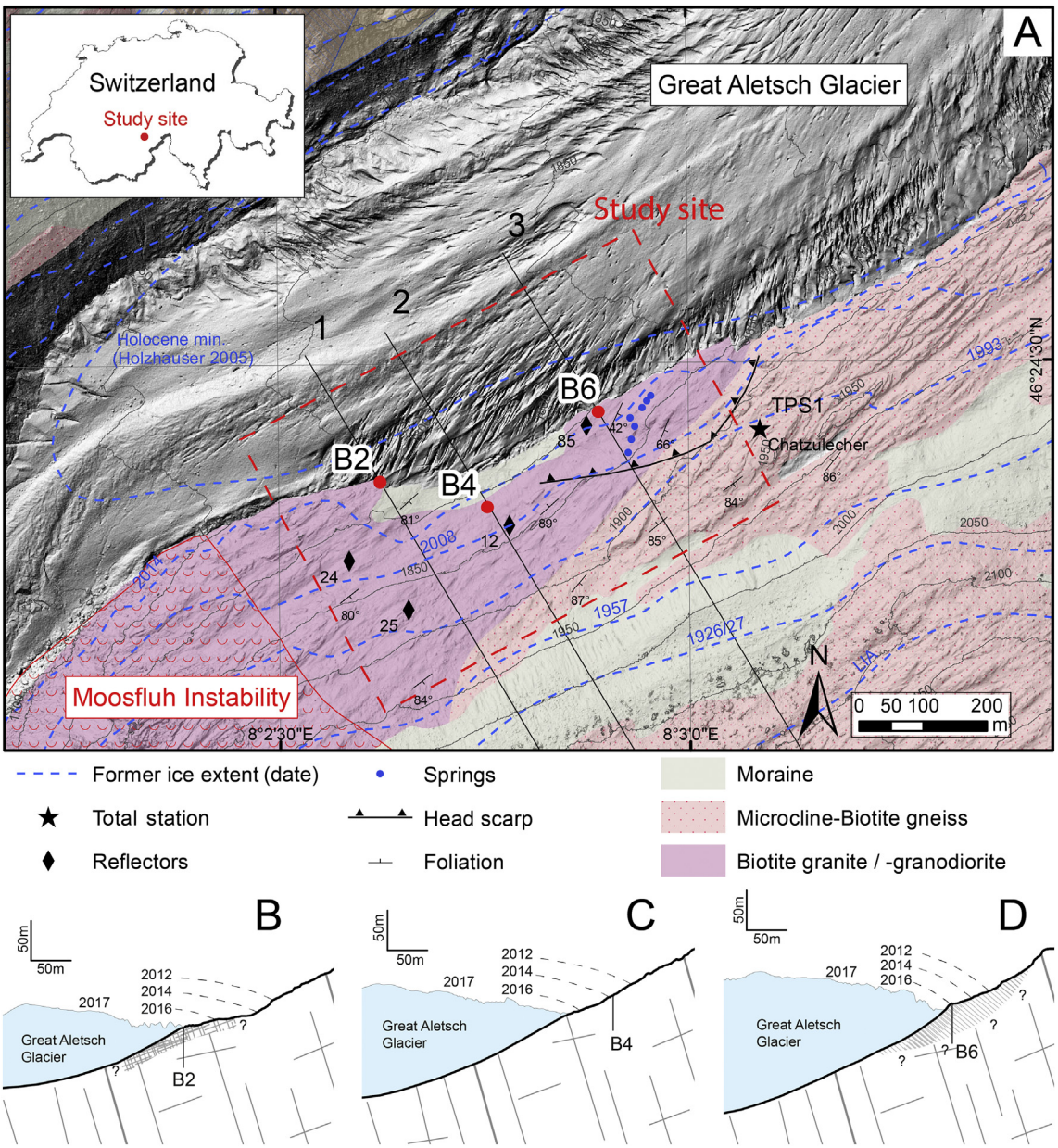

Fig. 3. A: Map view of the three borehole locations (B2/4/6, red dots) alongside the Great Aletsch Glacier tongue in Autumn 2017 and indication of the extent of the Moosfluh rock slope instability. The geological map from Steck (2011) was expanded down to the current glacier extent in our study area because, during their mapping campaign, this area was still ice-covered. The maximum LIA ice extent is well constraint by lateral moraines in the study area, and the Holocene minimum ice extent is shown as proposed by Holzhauser et al. (2005). The illustrated lateral glacial extents between 1926 and 2014 were digitized from aerial photographs by Glueer et al. (2020). B-D: Cross-sections cutting through the three borehole locations showing the glacial- and rock surface measured in the year of installation (2017) and the dashed lines indicate the lateral ice extent and approximate glacial height at the indicated year (DEM reproduced with permission of swisstopo (JA100120)). The shaded area in cross-section B indicates the stronger fractured surface layer (cf. Fig. 4), and the hatched area in cross-section D illustrates the dormant or relict landslide at B6 location. The locations of all other monitoring equipment close to our study site, including the GNSS sites and second total station, are provided in Glueer (2019).

three vertical (B2, B4, and B6, Table 1) and one inclined borehole (B3, Table 1) could be completed successfully.

At the first drilling location, the drilling rod got jammed while drilling the inclined borehole (B1, Table 1), so it had to be abandoned. At the third drilling location (B5, B6; Table 1), unstable borehole conditions were encountered. Therefore, perforated PVC casings were inserted directly after drilling in order to keep the boreholes open until the sensors could be installed. The installation of a PVC casing was accomplished in the vertical borehole B6 but not in the inclined borehole B5 (see Table 1). Before installing the permanent monitoring system, the successfully completed vertical boreholes were logged with geophysical and hydrogeophysical probes to characterize the rock mass and its hydrogeological parameters. The conducted logs and main results are summarized in Table 2. Borehole televiewer images show a strongly fractured rock mass at B2 with several open fractures, especially in the upper 20 m, whereas the rock mass at B4 is relatively intact, containing fewer and mainly closed fractures (see Fig. 4). Due to unstable borehole conditions, no extensive logging could be conducted in B6. The three vertical boreholes (i.e., B2, B4, and B6) were used for the installation of a borehole monitoring system described in Section 3.1.2, whereas the only successfully completed inclined borehole B3 was secured with a perforated PVC-casing and saved for future investigations.

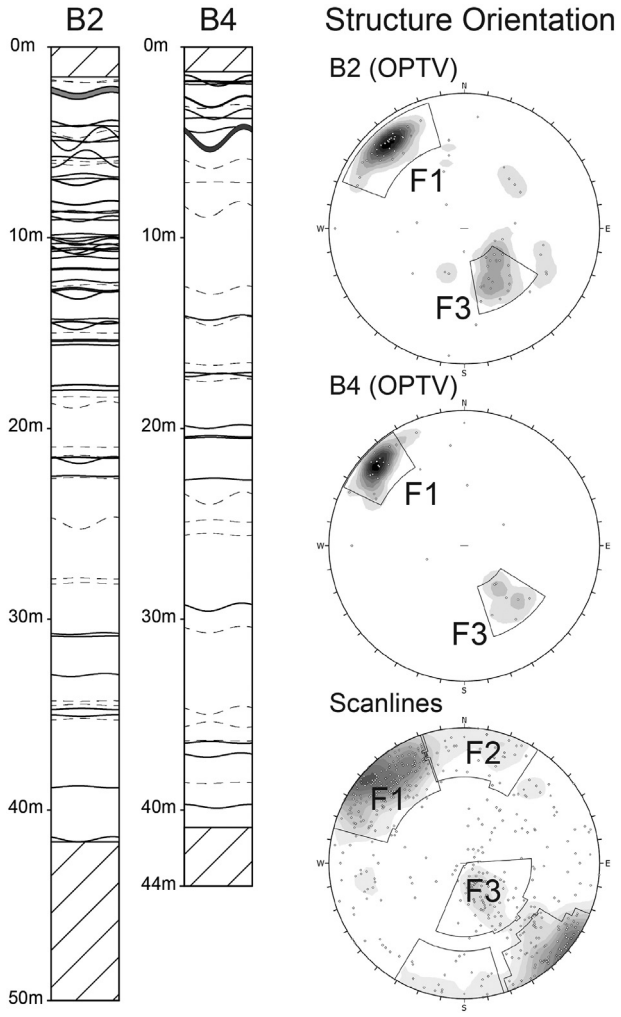

Fig. 4. Left: Structure logs from the optical televiewer (OPTV) survey in B2 and B4 (Location see Fig. 3). In borehole B6 no optical televiewer survey could be conducted because of unstable borehole conditions (cf. Section 3.1.1). The solid lines in the structure log indicate major discontinuities such as open joints, filled joints, and sheared and fractured zones, whereas the dashed lines indicate minor discontinuities (e.g., closed or healed joints). Hatched areas in the logs indicate depth sections with no optical televiewer data. Right: Structure orientations from optical televiewer log analysis and scanline mapping at surface outcrops in the study area. Surface structure data is compiled from 18 scanlines containing 533 discontinuity measurements.

3.1.2. Monitoring systems

High-resolution axial strain is recorded with FBG (Fiber Bragg Grating) strain/temperature sensor chains of 5 m base-length installed in each of three vertical boreholes (B2, B4, and B6). Horizontal strain components along these boreholes are recorded with biaxial SAA (Shape Accel Array) in-place inclinometer chains of 0.5 m base-length. These sensor chains include temperature sensors with a 1 m downhole spacing. Two of the three boreholes have functioning piezometric pressure sensors installed in a 1–2 m long sand filter at each borehole end. In B4, a modular rod extensometer chain with 10 m base-length is installed. Table 3 shows a summary of the installed borehole sensors, type, range, and accuracies. The sensors have recorded all parameters since fall 2017 at hourly intervals. Temporary downtimes of individual sensors that caused data gaps in the monitoring time series are discussed in Section 4.2. The instrumentation was accomplished by a collective work of two specialist companies for geotechnical monitoring. The SAA in-place inclinometer chain, the temperature sensor chain, and the pressure sensor are connected to a local data logger that contains an internal battery and a GSM data transmission unit that allows local data storage and transmission. The hourly measured data is automatically uploaded to an FTP server once per day, which allows data access from the office.

Fig. 5A shows the setup of the borehole monitoring system, a schematic sketch of the sensors in the boreholes (Fig. 5B), and cross-sections through the individual boreholes (Fig. 5C).

The FBG data acquisition system (DAS) consists of an FBG interrogator, a specially configured on-site computer with the FBG data recording software (Enlight by Micron Optics), the power supply (two 230 Ah batteries and a solar panel with two monocrystalline 165Wp modules), and a mobile access router for data transmission (see Fig. 2D). To reduce energy consumption, which is especially important in wintertime, the FBG system is controlled by a timer that provides power supply to the system during only 9 min per hour and initiates the measurement. This FBG DAS is located close to the central borehole location B4 (see Fig. 3) and connects to the FBG sensor chains of the individual boreholes with a reinforced fiber optical cable. The principles of operation of FBG strain sensors for geotechnical monitoring are described in the literature (e.g., Morey et al., 1990; Zhu et al., 2017).

For the current monitoring application, ten pre-strained, long gauge FBG strain sensors of nearly 5 m base length with integrated temperature compensation were installed in series down each of the boreholes. The pre-straining of the sensors was accomplished by fixing them to a stiff PVC injection pipe prior to insertion into the borehole (see Fig. 5B). For measuring the FBG sensors, a Micron Optics SM130 interrogator is used. The static hourly strain measurements are gained by measuring for approximately 30 s every hour and averaging the recorded strain readings to improve the precision. The improvement of the precision is proportional to the square root of the number of measurements (N) used for averaging (Smith, 1997). Thus, averaging of $N = 40$ measurements recorded in the 30 s leads to an improvement of the precision by a factor of $\mathrm{sqrt}(N) \approx 6.3$, which results in a precision of below 1 με for our setup.

The installed SAA in-place inclinometer chains are accelerometer-based sensor arrays with rigid 0.5 m long segments separated by flexible joints. Each of the segments contains three accelerometers that measure the tilt relative to gravity along the X, Y, and *Z*-axes. Every second segment additionally comprises a temperature sensor that is used for the internal correction of the segment length due to thermal expansion. The sensor chain was inserted in a PVC conduit that is grouted in the borehole. The bidirectional horizontal displacement is calculated with the tilt information in two horizontal directions and the segment length.

Table 1
Summary of the drilling works. All boreholes were destructively drilled with a borehole diameter of 101 mm and flushed with compressed air.

	Coordinates (lat/long)	Elevation [masl]	Drilling inclination	Depth	Date completed	Additional info
B1	46.405417/8.042693	1786	45°	19.0 m	07.08.2017	Drilling rod jammed -> abandoned
B2			90°	50.3 m	08.08.2017	Completed without issues; stable borehole
B3	46.405045/8.044873	1813	45°	54.0 m	10.08.2017	Completed without issues; stable borehole; PVC-casing installed to keep borehole open
B4			90°	44.4 m	14.08.2017	Completed without issues; stable borehole
B5	46.406383/8.047138	1808	60°	40.5 m	27.09.2017	Borehole unstable -> re-drilling -> installation of PVC casing not possible
B6			90°	50.0 m	26.09.2017	Borehole unstable -> re-drilling -> perforated PVC-casing successfully installed

Table 2
Summary of the conducted logging works in the three vertical boreholes. In the inclined borehole B3, no successful logging could be performed due to friction along the rugged borehole walls. In B6, only borehole fluid logging could be carried out through the perforated PVC-casing.

	Optical televiewer probe	Caliper probe	Heat pulse flow meter	Fluid electric conductivity/temp. log	Pumping/injection test	Main results
B2	Yes	Yes	Yes	No	Yes	Strongly fractured upper part of the borehole with open joints often filled with fines; discontinuity orientations (see Fig. 4); transmissivity in the upper 15 m of the borehole high (~ 10^{-3} m^2/s) and in the lower part around ~10^{-6} m^2/s
B4	Yes	Yes	Yes	Yes	Yes	More intact rock mass with mainly closed or low aperture fractures; discontinuity orientations (see Fig. 4); transmissivity between 9 m and 44 m borehole depth ~10^{-6} m^2/s with higher assumed values in the top layer; major transmissive structure at 29.4 m depth and minor transmissive structures at 19.5 m, 25 m, and 39.8 m
B6	No	No	No	Yes	Yes	Transmissivity between 14 m and 50 m depth ~10^{-5} m^2/s with higher assumed values in the top layer; major transmissive structures at 35.5 m and 43 m depth and minor transmissive structures at 29.5 m and 47 m

To ensure the durability of the system and minimize the exposure of the fiber optical cable to environmental effects (e.g., snow creeping, avalanches, debris flows, and rockfalls), the cable was either buried into the moraine soil, fixed onto bedrock, or suspended over critical sections such as creeks or debris flow channels. The borehole heads and the local dataloggers are secured by concrete chambers that are anchored to the ground (see Fig. 2C).

3.1.3. Borehole completion and grouting

After sensor installation, and to assure a good coupling of the sensors to the rock, the three instrumented boreholes were fully grouted with an expanding cement-bentonite mixture. The grouting of B2 and B6 was challenging because of the risk of losing grout through highly transmissive structures. In B2, this problem was prevented by inserting a geotextile prior to the sensor installation. However, in B6, no geotextile was used for the grouting because this would have led to a coupling of the sensors only onto the PVC casing and would not have fixed the sensors directly onto the rock. Therefore, more than once the borehole volume of the grout was lost through transmissive structures during injection and only the lowermost 23 m of the borehole (i.e. 27 m to 50 m depth) could be filled in the first grouting campaign in 2017. The remaining uppermost 27 m of the borehole B6 were then successfully grouted during a second campaign in August 2018.

3.1.4. Surface deformation monitoring

Continuous surface deformation has been measured at the study site since 2013 and is used to compare continuous displacements at the surface with displacements measured at depth with the borehole monitoring system. The monitoring array includes a robotic total station (TPS 1), and a GNSS receiver (Frukacz et al., 2017; Glueer, 2019). This total station monitors the position of over 80 reflectors, and locations 12, 24, 25, and 85 are relevant to the present study. The reflector and TPS 1 locations are shown in Fig. 3.

Only nighttime measurements from the TPS station were used in order to reduce atmospheric artifacts and temperature variations. Offsets caused by maintenance of the total station are also corrected. A daily solution is built by first removing outliers at the 4 standard deviation level, and then low-pass frequency filtering of the angular measurements (horizontal and vertical) for white noise reduction. Calculated coordinates relative to the TPS station are then corrected for the motion of the monitoring station itself, with low-pass filtered continuous Global Positioning System (cGPS) data. The cGPS data are processed independently, using a protocol described by Limpach et al. (2016).

4. Results and interpretation

In this section, monitoring data collected between October 2017 and October 2019 (i.e., the first 2 years of monitoring) is provided and discussed in order to show its value to investigate the thermo-hydro-mechanical coupled processes introduced in Section 1. More specifically, the monitoring system should enable quantification of displacements at the borehole and fracture scale caused by permanent changes in thermal and hydraulic boundary conditions due to ice retreat and cyclic thermo-hydro-mechanical loads originating from daily and seasonal fluctuations in the rock slope and the ice body.

4.1. Borehole grouting effects

The monitoring data time series during the first few weeks after installation in October 2017 are not used for interpreting the in-situ conditions of the rock slope. This is because these measurements contain artifacts related to the hardening process of the grout in the borehole, such as temperature anomalies due to the exothermal reaction and borehole internal displacements. Under the given borehole conditions, temperature peaks of the hardening process normally occurred

Table 3
Characterization of the sensors deployed in the three research boreholes B2, B4, and B6. All sensors measure at an hourly time interval. Accuracy and precision values shown here are provided by the manufacturer.

Sensor	Parameter	Type	Range	Segment length, base length, sensor spacing	Accuracy (A), Precision (P)
FBG sensors	Axial strain	SC-01 (Sylex Fiber Optics s.r.o)	±5000 με	B2: 4.81 m B4: 4.31 m B6: 4.83 m	A: 11 με (<0.18% FS)[a] P: 6 με (<0.10% FS)[a]
SAA inclinometer chain (biaxial)	Horizontal displacement Temperature	SAAF500–003 (Measurand Inc.)	± 60° w.r.t. vertical −35 °C to 60 °C	0.5 m 1 m	A: ±0.25 mm –
Piezometric pressure sensor	Pressure	PA-27XW 10 bar (Keller AG)	0–10 bar	–	A: < ±3.5 mbar
Extensometer rod (only in B4)	Axial strain	M-RHX (Solexperts AG)	± 50 mm	10 m	A: 0.1 mm (0.2% FS)

[a] ±3000με assumed as maximum strain range for the current project.

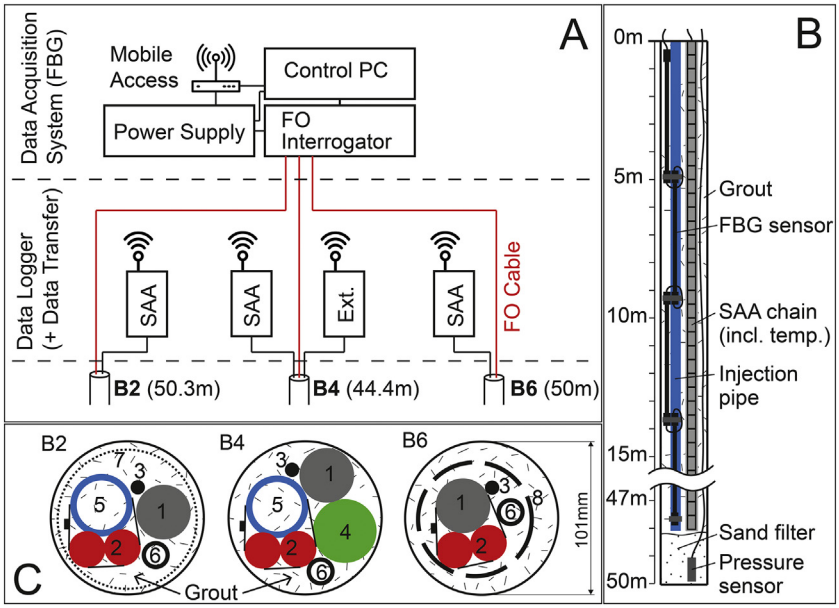

Fig. 5. A: Setup of the borehole monitoring system; B: Schematic sketch of the sensor deployment within a borehole; C: Cross-section through the boreholes B2, B4, and B6 drawn in scale. 1: SAA inclinometer chain; 2: FBG strain/temperature sensors; 3: Pressure sensors; 4: Extensometer rod; 5: Injection tube; 6: Injection pipe; 7: Geotextile; 8: Perforated PVC tube.

approximately two days after the grout injection into the specific interval. Subsequent to this peak, the temperature sensors in the lower portion of the boreholes approached a constant value within less than two months. After this time (i.e., from December 2017 onwards), the measured temperatures are considered to reflect in-situ subsurface temperature values without disturbance from the grouting process.

4.2. System reliability

Continuous monitoring in an extreme alpine environment is challenging mainly because of the reduced accessibility during the long winters with snow heights up to a few meters. Fig. 6 shows a summary of the time when the individual sensors were reliably measuring. The SAA inclinometer, temperature and pore pressure data in B4 and B6 have been almost continuously recording since October 2017. The infrequent data gaps in these monitoring time series were related to battery issues that could be fixed within a few weeks. The FBG system has been reliably recording since July 2018. Extreme environmental conditions were the cause of two further data gaps, one at all sensors of B2 (label 'a' on Fig. 6) and one at the FBG system (label 'b' on Fig. 6). The four-month data gap at borehole B2 sensors was related to a re-advance of a side finger of the Great Aletsch Glacier that overrode this borehole location and disrupted the borehole sensor chains from the loggers in March 2018. In August 2018, these borehole sensors could be reconnected to the loggers that were newly placed at a safe location, and a ramp was cemented over the borehole location to prevent the cables from being destroyed during a possible (but not expected) future winter re-advance of the glacier's side finger. In January 2019, a winter storm took down the solar panel of the FBG DAS and caused a data gap of 1 month in the FBG data (Fig. 6, label 'b'). The pore pressure sensor of B2 has not been working properly since the time of installation, either due to a malfunction of the sensor or because it was accidentally grouted.

4.3. Temperature data

A full annual subsurface temperature cycle from 2018, containing monthly mean values measured in B2 and B4 is provided in Fig. 7. Additionally, the figure contains unwrapped images of the borehole wall illustrating the mapped structures from the optical televiewer log of the two boreholes. The temperature data of B6 is not shown because this borehole was still partly ungrouted until August 2018, and then the in-situ subsurface temperature field got further disturbed by the second grouting campaign.

In the B2 temperature plot, the monthly mean temperatures between April and July are missing. Although the complete year could

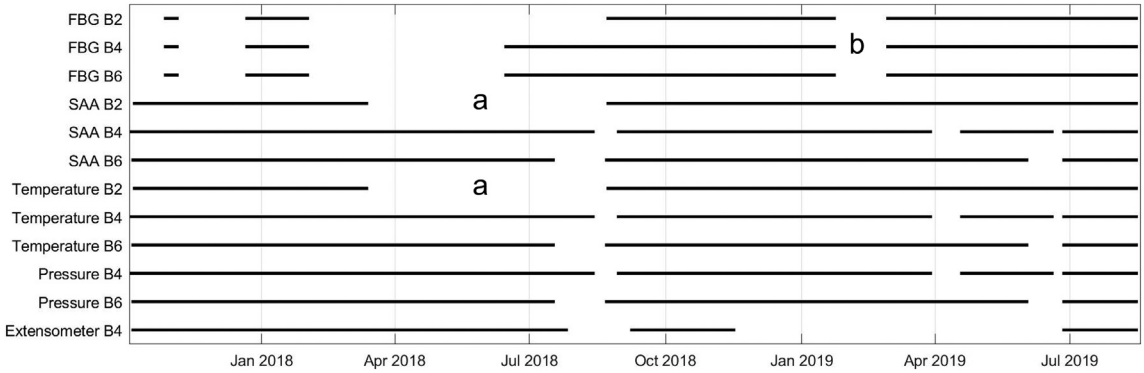

Fig. 6. Downtimes of individual sensors of the borehole monitoring system since the time of installation. Times, where the sensors were reliably working, are indicated with black lines, whereas gaps in the lines mean no useful data. The letter 'a' and 'b' denote time periods referred to in the text.

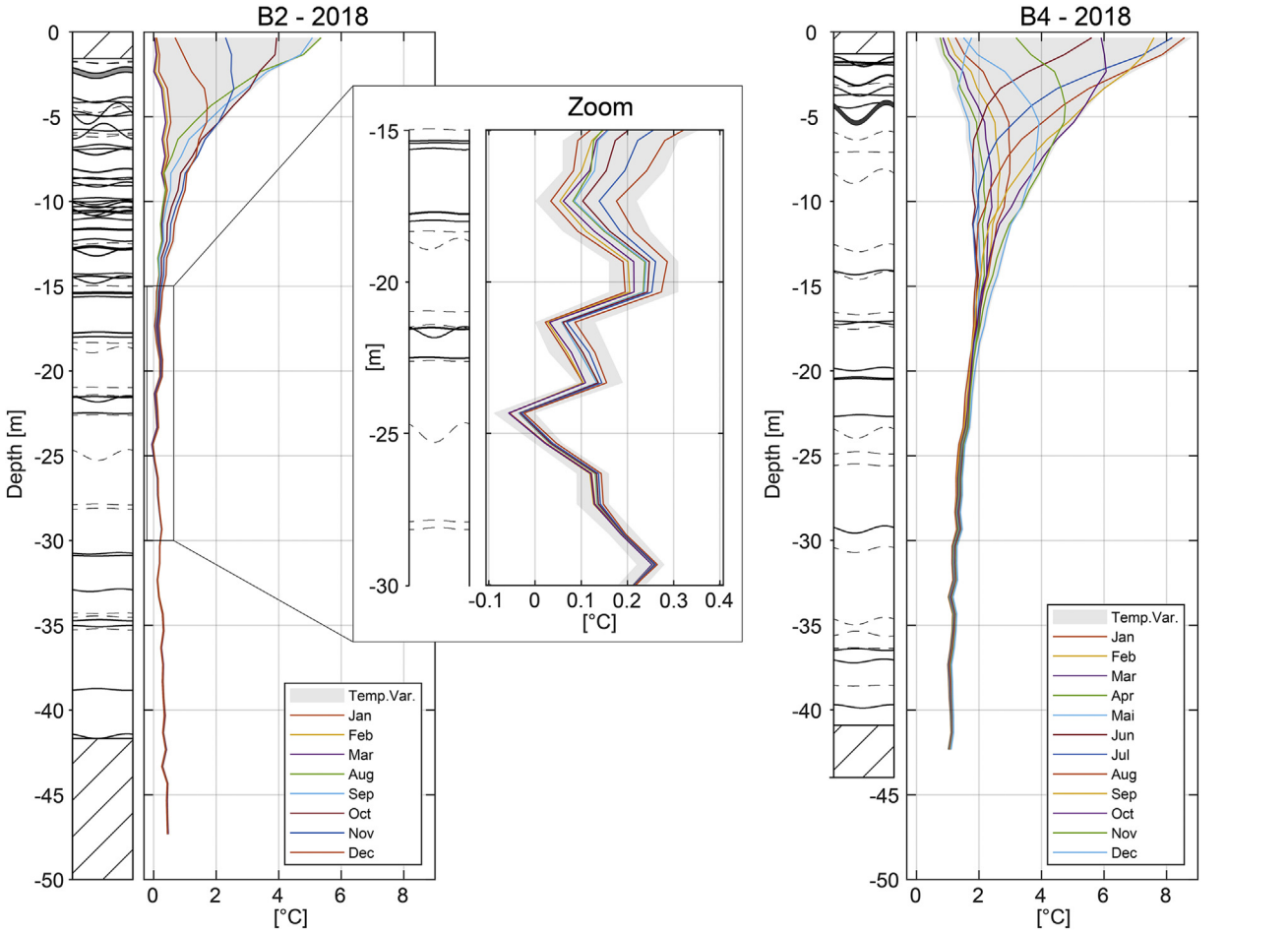

Fig. 7. 2018 monthly mean subsurface temperature profiles in research boreholes B2 and B4 with the absolute temperature range indicated in gray. The mapped discontinuities from the optical televiewer log in an unwrapped borehole wall visualization of B2 and B4 are provided to the left of the particular temperature data. Dashed lines in the structure log indicate minor structures (e.g., closed joints), whereas solid lines indicate major discontinuities (e.g., open fractures, filled fractures, fractured zones, and sheared zones).

not be measured at B2, the annual thermally active layer is considered to be captured well. This is because the maximum temperatures in B2 are clearly captured with the measurements in August, September, and October, and the annual minimum values are considered to be very close to the values of March (cf. B4 temperature data).

The temperature profiles of the two boreholes show a similar depth of the annual thermally active layer of around 17 m, however, with different amplitudes. The uppermost sensor of B4 (installed at about 0.33 m depth) shows an annual temperature variation of 8.2 °C, whereas, at B2 the amplitude at 0.33 m depth is only 5.3 °C. At B2, below the thermally active layer and down to a depth of about 25 m, the average temperature is close to 0 °C. Below this depth, the temperature linearly increases with an approximate rate of 0.2 °C/10 m depth. The B4 data show a decreasing temperature with depth below the thermally active layer with the lowest absolute value of about 1 °C at 42 m depth. The rate of this negative downhole trend, however, is not linear and decreases with depth. Superimposed to the general temperature profile, both boreholes show weak positive and negative temperature anomalies at specific depths (e.g., Fig. 7, in borehole B2 at 20 m, 24 m, and 35 m or in borehole B4 at 29 m and 33 m depth).

Typical undisturbed and conduction-dominated subsurface temperature profiles are expected to show a linear temperature increase with depth, with a temperature gradient controlled by the geothermal heat flux from the earth's interior (which is a product of the geothermal gradient and thermal conductivity of the rock) and surface temperature on the other side (Pollack, 1993). If other influencing factors (e.g., vegetative patterns, hydrological features, lateral heterogeneity, phase changes, or advective heat transfer) are assumed minor, deviations from such a quasi steady-state profile can be interpreted as surface temperature perturbations that penetrate into depth; positive deviations show a warming and negative deviations a cooling at surface, respectively (Pollack, 1993; Pollack and Huang, 2000).

The inverse temperature gradient observed in B4 is interpreted to reflect surface warming caused by the glacier retreat since summer 2014 that changed the surface temperature from relatively constant 0 °C below the ice to a mean annual ground temperature above 0 °C after exposure of the land surface to the atmosphere. Thus, the cold temperatures induced by more than one thousand years of ice occupation at this location are still preserved at depth. The subsurface temperature at this location is in a transient state, slowly adapting to a new mean annual ground temperature. It is assumed that the inverse temperature profile measured in this borehole is approaching a turning point somewhere below the borehole to a positive geothermal temperature gradient similarly as illustrated in figure 5 of Grämiger et al. (2018).

The shape of the temperature profile of B2 is different. Below 25 m depth, it shows a linearly increasing temperature with depth of about 0.2 °C/10 m, which agrees with the literature values of the geothermal gradient in the Aare massif of 23 °C/km (Rybach and Pfister, 1994). Sensors between 17 m (depth of thermally active layer) down to about 25 m depth show rock temperatures around 0 °C. We hypothesize that observed temperatures in this depth could be related to advective heat transport of cold water (close to 0 °C) that is directly connected to the glacial ice through the transmissive discontinuities in the highly fractured shallow subsurface. This because such low temperatures at a

depth of 17 to 25 m cannot be physically explained by conduction only, assuming approximately 0 °C at the ground surface (below temperate glacial ice) or even higher mean annual ground temperature after ice retreat.

The weak positive and negative temperature anomalies along both temperature profiles are likely caused by transmissive fractures conducting water (or air) at a different temperature compared to the surrounding rock. This hypothesis is supported by observation from optical televiewer images where the depth of fractures sometimes coincides with temperature anomalies (e.g., Fig. 7, B2 - zoom between 15 and 30 m, B2 at 35 m, or B4 at 29 m depth) or by interpretation of the fluid electric conductivity log that showed a conductive feature in B4 at 29 m depth. The results of the fluid electric conductivity logs are not shown in this publication.

4.4. Pore-water pressure data

Fig. 8 shows the pressure head from the two sensors installed at the end of borehole B4 and B6 at a depth of 43.75 m and 48.75 m, respectively. No pore-water pressure data can be provided for borehole B2 because this sensor is not working (see Section 4.2). The two sensor readings show a different pressure regime between the slope location (B4) and the location next to the glacier (B6) (see Fig. 3). At B4 - the slope location with approximately 50 m lateral distance to the 2017 ice margin - the pressure head shows an annual variation of about 15 m. The maximum head is reached directly after snowmelt infiltration in spring (i.e., April/May). After this main recharge period, pore pressure globally decreases over the course of the year, punctually interrupted by minor pore pressure rises linked to smaller recharge events following rainfall and small snowmelt events. From late autumn onwards, as soon as the precipitation is held back as snow on the surface and no more recharge occurs (black bar, Fig. 8), the pressure head decreases even faster. Some exceptions are related to heavy rainfalls in winter that probably infiltrate through the snowpack into the bedrock (see label a, Fig. 8).

At B6, which was drilled with only 5 m lateral distance to the 2017 ice margin and below a major groundwater seepage zone (Fig. 2), the annual variation of the pressure head is only around 4.5 m, lower than the annual amplitude measured in B4. The highest values again coincide with the timing of the main snowmelt infiltration in spring, and sometimes weak pressure reactions to rainfall can also be observed.

The two-year pore pressure history in B4 shows signs of a typical slope groundwater recharge-discharge regime (cf. de Palézieux and Loew, 2019) with a relatively strong annual pressure head increase during the main snowmelt infiltration period in late spring, and slow pressure recession during the course of the year interrupted only by significant rainfall and snowmelt events outside the main snowmelt period. The lower pore pressure variability in B6, initially located 5 m from the glacier, is likely related to its proximity to the relatively constant boundary conditions from the temperate glacier and possibly the seepage zone some tens of m upslope. Similar to the assumed englacial water pressure, B6 shows a relatively stable pressure head during winter and more variability during summer.

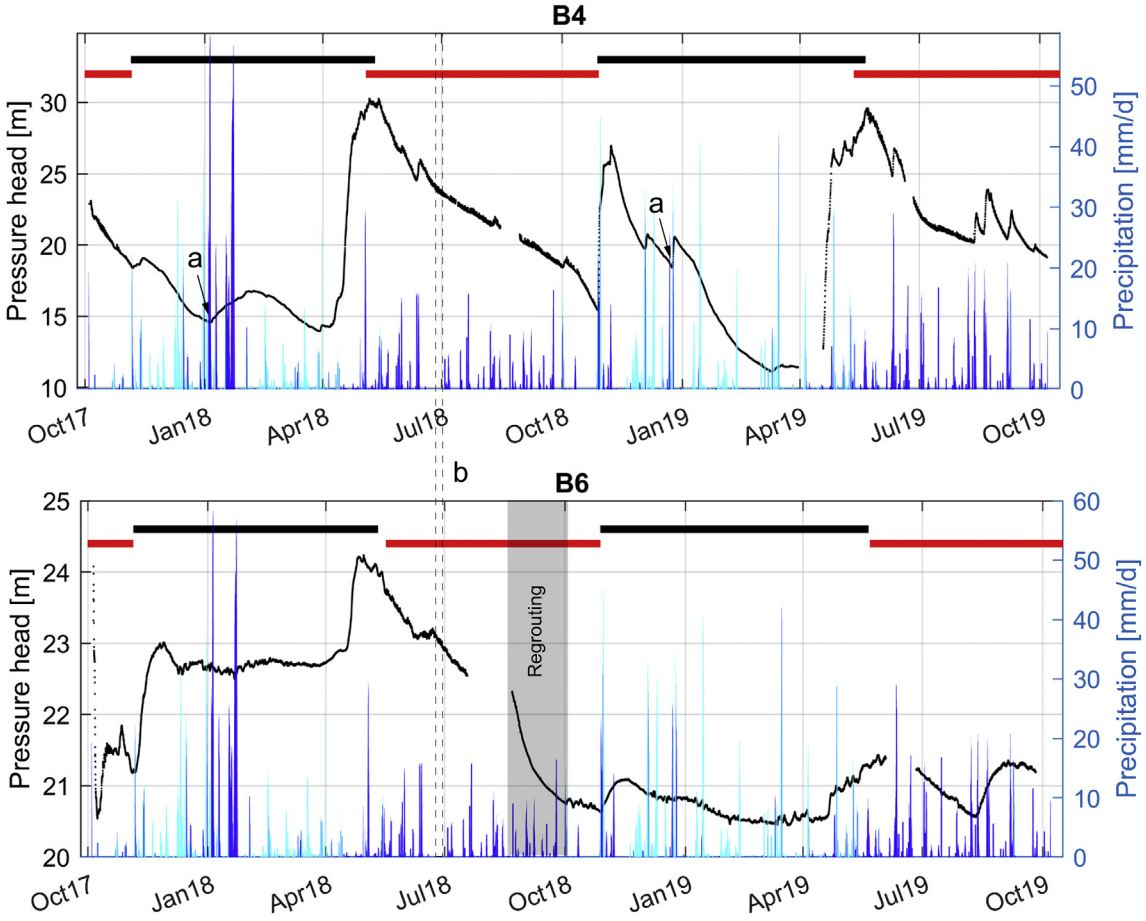

Fig. 8. Pressure head (above borehole end) from atmospherically corrected pressure data in B4 and B6. The vertical bars show the cumulative total precipitation data (per 24 h) provided by MeteoSchweiz from the weather station "Bruchji" (Valais) located approximately 6 km away from our study site. The cyan colored bars indicate precipitation that presumably occurred as snow (i.e., at surface temperatures below 1 °C at our study site (cf. Jennings et al., 2018)). The black horizontal bars indicate the time of the year when the slope was snow-covered, and the red horizontal bars indicate the time daily pressure fluctuations could be observed in the time series. Labels a indicate pressure head increases referred to in the text. Label b indicates the location of the presented data in Fig. 9.

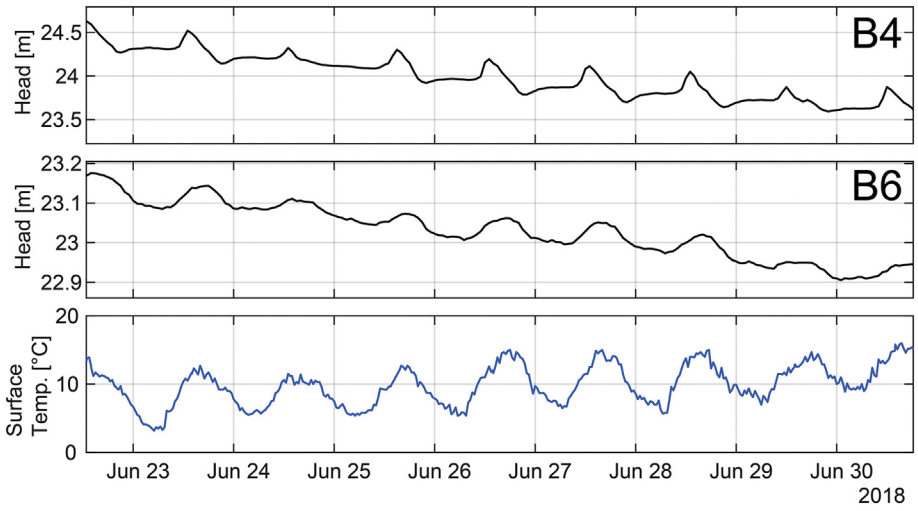

Fig. 9. Zoom on daily pressure signals in B4 and B6 plus surface temperature at the study site for interval b (Fig. 8) in late June 2018. The tick labels on the date axis are located at midnight.

In both boreholes, low amplitude daily pressure cycles can be detected from spring until fall but not in winter. The red horizontal bars in Fig. 8 indicate the timing of these daily pressure cycles, and Fig. 9 shows the detailed pressure signals in late June 2018. These diurnal pressure signals show maximum values in the afternoon and minimum during the night, correlated to variations in air temperature; however, often with a slight time shift that is not constant over time. The amplitude of the daily pressure head cycle varies between the two boreholes with approximately 20–30 cm in B4 and 2–5 cm in B6, respectively. Their amplitude stays relatively constant over the time of the year that they occur. These clearly detected daily pressure fluctuations could reflect a strongly attenuated pressure signal of daily glacial meltwater cycles diffusing into the slope. The different shapes of the diurnal signals (i.e., amplitude and phase shift) might be related to variable hydraulic properties of the bedrock at the two borehole locations. The irregular shape of the daily cycles in borehole B4 (e.g., June 28th and 29th) might also suggest that signals of different origins could be superimposed.

4.5. Displacement data

This section illustrates the different observed displacement characteristics, magnitudes, and potential drivers for the deformation in the instrumented, glacier adjacent rock slope. Annual reversible surface displacements at these slopes are on the order of 10–20 mm, and the irreversible displacements are about a factor 10 smaller (Glueer, 2019). The surface displacements are interpreted as the integrated displacements along individual discontinuities at depth. Numerical simulations of Grämiger (2017) suggest that these displacements result from thermo-hydro-mechanical coupled effects of annual groundwater and temperature cycles superimposed to long-term stress changes due to glacial retreat (i.e., mechanical ice unloading and long-term temperature and groundwater changes). The irreversible portion of the displacement is thought to reflect progressive damage that occurs along individual, critically stresses fractures driven by these fatigue processes. Magnitudes of irreversible displacements along individual discontinuities were modeled on the order of 10 to 100 μm per year. For the differentiation between reversible deformation and irreversible deformation, the measured deformation signal is compared to potential drivers for stress perturbations such as temperature or pore-water pressure fluctuation. The portion of the deformation that remains after the perturbation is defined as irreversible deformation (or damage) whereas reversible deformation recovers after the perturbation. These stress perturbations occur at diurnal to annual timescales in the presented data (cf. Sections 4.3 and 4.4).

The investigation of the staged evolution of rock slopes leading to the formation of rock slope instabilities, such as toppling or sliding slopes, can be based on kinematic analysis of fracture reactivation triggered by various loading mechanisms (Gischig et al., 2011a, 2011b). In Section 4.5.3, we show how our data set will therefore be used to integrate information from the subsurface structure logs and the horizontal and vertical displacement monitoring data. This will allow us to identify displacement vectors along individual structures in order to gain an understanding of the slope kinematics and the most critical fracture orientations reacting to the environmental drivers in the given stress field.

4.5.1. FBG strain sensor data

Fig. 10 shows the readings of the temperature corrected hourly strain measurements of all FBG sensors in borehole B4. FBG strain data from boreholes B2 and B6 are not provided because of limited space. Strain recordings in these two boreholes, however, show similar displacement characteristics and reactions on precipitation and infiltration events as the presented data from B4. The static strain values are calculated by averaging over hourly dynamic measurements of approximately 30 s duration. In the first 14 months of FBG strain data measurements, various displacement characteristics were identified at a wide range of strain amplitudes from below 1 με (or ~4 μm) up to single strain events larger than 50 με (or ~0.2 mm) (e.g., Fig. 10, label a). We measure both extension and contraction in a reversible and irreversible manner as well as a combination of the two. Deformation can be observed as abrupt steps that occur between two measurements (i.e., within 1 h) at a single sensor (e.g., Fig. 10, label b) or at several sensors simultaneously (e.g., Fig. 10, label c). In general, distinct short-term strain events (hours to few days), which may correspond to individual slip events, often coincide with precipitation events (cf. Fig. 10 events a-d). The two major displacement events in our current FBG time series temporally coincide with two major infiltration events. The first event occurred during a very strong rainfall in late October 2018 that was able to melt the early snow cover in the area (Fig. 10, label d), and the second one occurred during the main snowmelt period in spring 2019 (Fig. 10, label e). Deformations during these two events were clearly detected at most of the sensors and normally occurred as a combination of reversible and irreversible displacements. In addition, long-term continuous displacements are observed in the time series, which occur over several hours, days, or months.

In Fig. 11, a zoom of the three lowermost FBG sensors in B4 (from 30.4 to 43.4 m depth) during July 2018 is provided (cf. Fig. 10, label f). At these sensors, among others, clear daily strain cycles with a variable amplitude of around 5 με can be observed. These daily cycles do not occur during winter, are measured in all the three boreholes, but not

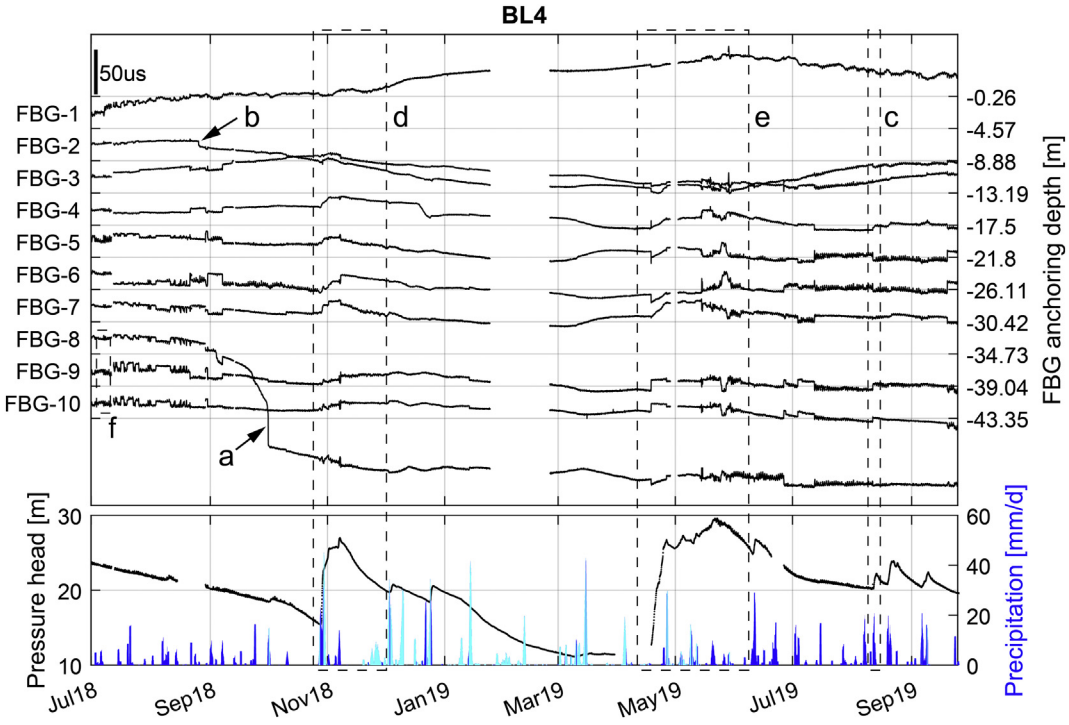

Fig. 10. The black lines in the upper plot show a visualization of the temperature corrected strain data of the individual 4.31 m base-length FBG sensors installed in borehole B4. The strain data of each sensor is plotted in the center of the specific depth interval, and the vertical axis ticks correspond to anchoring depth of the FBG sensors. Positive strain means elongation and negative strain compaction of the sensor, and the strain scale is provided on the top left in microstrain (με). Additionally, the pressure head measured in the borehole is shown with the blue line in the lower plot. The vertical bars in the lower plot show the cumulative total precipitation data (per 24 h) provided by MeteoSchweiz from the weather station "Bruchji" (Valais) located approximately 6 km away from our study site. The cyan colored bars indicate precipitation that presumably occurred as snow (i.e., at surface temperatures below 1 °C at our study site (cf. Jennings et al., 2018)).

at all of the sensors, and they are generally more strongly pronounced at deeper sensors. Further, the strain cycles at the different sensors are in phase but can show an opposite strain direction and sometimes stop abruptly or change strain direction e.g., after simultaneously occurring strain events such as event 'c' in Fig. 10.

The observed daily strain cycles in Fig. 11 show a positive or inverse correlation to surface temperature and pressure head measurements in the borehole. Days with lower surface temperature and pressure amplitude (e.g., July 5th and 6th) cause a smaller amplitude in both the pressure and strain signal. We hypothesize that direct correlations of the strain signal might be related to fracture opening (or shear dilation) in the given interval due to water pressure increases. Inverse correlations, in contrast, could be explained by pressurized transmissive structures outside of the measured interval that cause a compression in the FBG interval. Similar couplings between adjacent strain monitoring intervals have also been observed in other experiments (e.g., Krietsch, 2019).

4.5.2. SAA inclinometer chain data

Results of the horizontal displacements measured with the SAA in-place inclinometer chain of borehole B4 in the year 2018 are provided in Fig. 12. Inclinometer displacement data of boreholes B2 and B6 are not shown because of limited space. Both, B2 and B6, show similar displacement characteristics as presented below using the example of B4. Although the resolution of these sensors is not as high as with the FBG

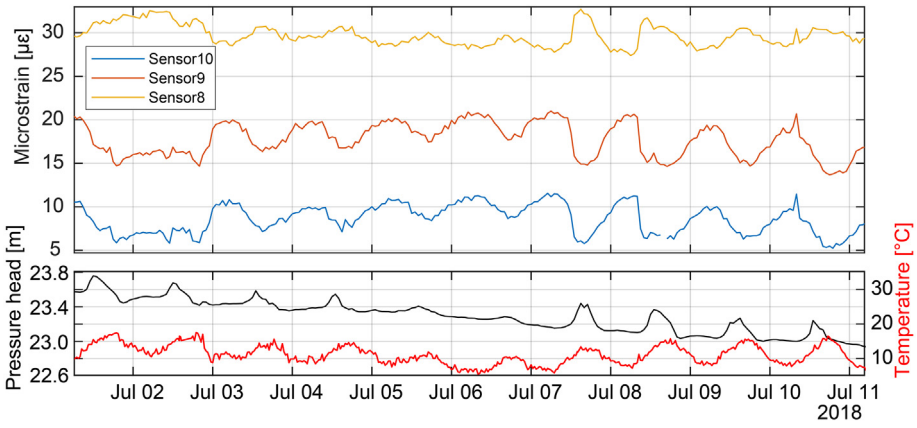

Fig. 11. The upper plot shows an example of daily strain cycles measured in B4 at the three lowermost FBG sensors (30.4 to 43.4 m depth). The strain data is provided with a 10 με offset between the sensors for better visualization. The lower graph illustrates the pressure head measured in B4 and the surface temperature measured at the study site. The tick labels on the date axis are located at midnight.

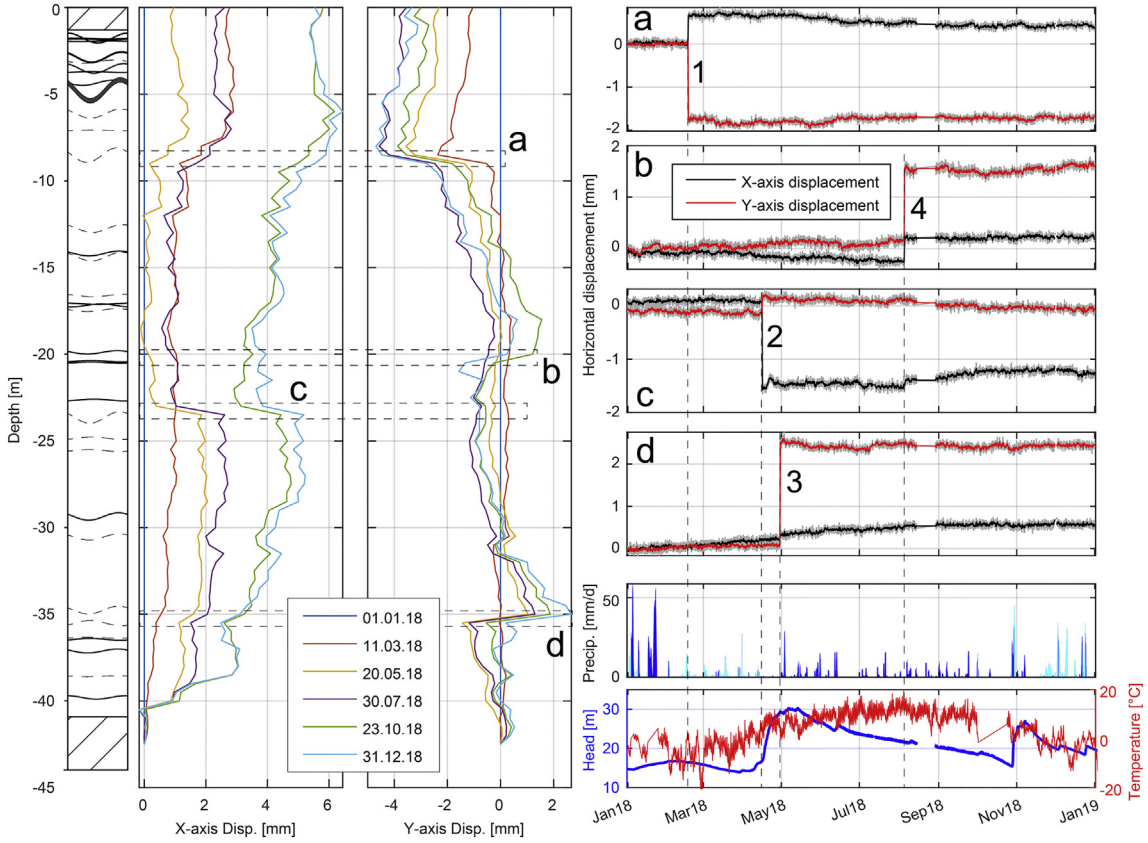

Fig. 12. Left: SAA inclinometer chain data of B4 in 2018 showing the cumulative displacements of each segment from the borehole end up to the surface in both horizontal directions vs. borehole depth (X+ direction equals an azimuth of 194° and Y+ direction of 104°). Further, the mapped discontinuities from the optical televiewer log in an unwrapped borehole wall visualization are provided. Right: Continuous sensor readings of specific depth segments in X and Y direction using a moving mean filter over 10 measurements and the raw data provided in gray in the background (a, b, c and d). Numbers 1–4 indicate rapid displacement events referred to in the text. Below the continuous displacement data, precipitation data, surface temperature data of the study site, and the atmospherically corrected pressure head measured in borehole B4 is shown. The vertical bars in the precipitation plot show the cumulative total precipitation data (per 24 h) provided by MeteoSchweiz from the weather station "Bruchji" (Valais) located approximately 6 km away from our study site. The cyan colored bars indicate precipitation that presumably occurred as snow (i.e., at surface temperatures below 1 °C at our study site (cf. Jennings et al., 2018)).

system, clear reversible and irreversible displacements can be recorded at this location. Using a moving mean filter over 10 measurements reduces the high-frequency noise and allows for the detection of sudden displacement events down to about 0.1 mm (see Fig. 12, graphs to the right). Visualization of horizontal displacement data in a cumulative plot highlights specific depths with high activity (i.e., steps in Fig. 12 (left graph) at depth a-d). These locations usually coincide with the depth of mapped structures in the optical televiewer log.

The inclinometer system detects both slow/continuous and rapid displacements. Rapid displacement events at specific depth were measured at individual magnitudes of up to about 2.5 mm (e.g., events 1–4 in Fig. 12). The existing data shows that the timing of some of the displacement events coincides with potential climatic triggers. For example, event 2 and 3 (Fig. 12), occurred during the strong pressure head increase due to snowmelt infiltration in spring 2018. Other sudden displacements coincide with extreme summer surface temperatures (e.g., Fig. 12, event 4 at depth b and c).

Horizontal surface displacements at reflector 12 and the cumulative horizontal displacements of the inclinometer chain at B4 were compared between April and December 2018 (see Fig. 13). Borehole B4 data was used for the comparison with surface displacement data, because it is the only one of the three boreholes that has a reflector close by with a continuous data series that is adequate for comparison. Both show a similar displacement behavior (in orientation and timing) with a mainly reversible component in downslope direction and a slope parallel displacement component oriented in direction SW (i.e., down valley and in the direction of the Moosfluh slope instability). The magnitudes of the slope parallel displacement components are similar for both systems. However, the magnitude of the reversible downslope displacement of inclinometer B4 is only about a quarter of the magnitude of the reflector. This could indicate that the deformation process leading to the reversible downslope displacement occurs also along discontinuities that are deeper than borehole B4 (44 m), and the slope parallel displacement in the monitoring period is happening mainly along discontinuities in the uppermost 44 m. The reversible, downslope oriented displacement temporally coincidences with the annual main pressure head increase due to snowmelt infiltration and its subsequent recession during summer. Therefore, this displacement likely reflects a mainly elastic response of the slope to annual groundwater table fluctuations. These elastic responses to groundwater fluctuations in alpine valley flanks have been observed in other studies (e.g., Hansmann et al., 2012).

4.5.3. Slope kinematics

Some heavy rainfalls cause clear displacement events that can be observed simultaneously in both the FBG sensor and the SAA inclinometer chain data within the same depth interval (e.g., in borehole B2, Fig. 14, event 1). During event 1, a positive axial strain (i.e., extension) of about 40 με (or ~ 0.19 mm) was observed at the FBG sensor 3 anchored between 10.38 m - 15.19 m depth. Within this depth interval, four of the eleven inclinometer sensors (circled in Fig. 14) also detected horizontal displacements with individual amplitudes between 0.1 and 0.2 mm. In order to infer actual fracture kinematics and mode of re-activation, the two horizontal SAA and the vertical FBG displacement have to be

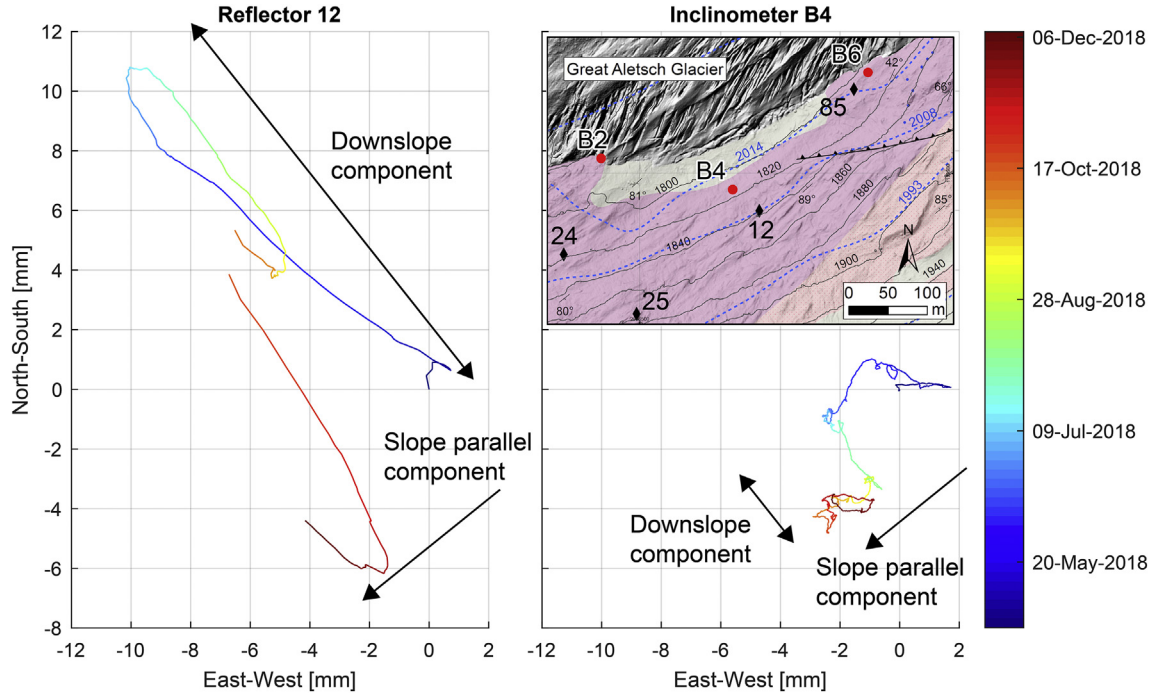

Fig. 13. Visualization of the horizontal surface displacements at reflector 12 (black diamond symbol on map) measured with the TPS 1 station (left graph) and the cumulative horizontal displacements measured with the SAA in-place inclinometer system in borehole B4 (red dot) (right graph). On the top right, a zoom of the map in Fig. 3 is provided to show the local slope direction and the location of the borehole B4 and the reflector 12.

combined with the fracture orientation from televiewer logging. For geometrical reasons, normal opening and reverse shearing mechanisms cause positive strain (or extension) at the FBG sensor, whereas negative strain measurements (i.e., contraction of the sensor) will originate from normal closure or normal shearing of fractures (Fig. 15). In addition, the measured strain magnitude not only depends on the actual fracture displacement but also on the angle between the fracture and the sensor (see Fig. 15). This angle-dependent ratio between actual fracture displacement and strain measured at the sensor can be calculated geometrically using the law of cosines. In a similar manner, the measured horizontal displacement of the SAA chain only reflects a fraction of the total fracture displacement.

One possible interpretation of the actual fracture kinematics is illustrated with blue arrows in Fig. 14. This interpretation includes normal shearing and opening between 10 m and 11.5 m depth and reverse shearing and possibly closing at around 13 m. Although such an interpretation of 3D fracture displacements is currently uncertain, longer time series will allow a clearer identification of active structures and their kinematic behavior.

5. Discussion

5.1. Subsurface temperature and pore-water pressure regime

The temperature sensor chain revealed the effect of the lateral ice retreat and annual temperature cycles on the transient subsurface temperature regime. The annual thermally active layer in the slope above the ice elevation is around 17 m deep at our study site and the negative thermal gradient (i.e., cooling downwards) observed in borehole B4 likely reflects a transient temperature signal as the slope adapts to a new, warmer mean annual ground temperature following ice retreat.

The pressure sensors allow us to characterize the pore-water pressure in a fractured, crystalline rock slope adjacent to a warm valley glacier. Seasonal pore pressure variations are regulated by (1) snowmelt recharge during the main snowmelt period in spring, (2) recharge from rainfalls and snowmelt events outside the main snowmelt period, and (3) effects of englacial water in the temperate glacier. The data shows low annual pressure head variability (~ 4 to 5 m) and relatively stable values during wintertime close to the glacier (borehole B6). This low variability is likely related to the proximity of the borehole to the relatively constant glacial pressure boundary condition (i.e., the reservoir effect of temperate glaciers). In borehole B4, located further from the glacier, the pressure head shows stronger annual fluctuations (~ 18 m) with maximum values after snowmelt infiltration and a subsequent depletion over the course of the year, interrupted by strong rainfalls or additional minor snowmelt events. Further, we measure weak daily pressure head fluctuations of up to a few decimeters in amplitude in the rock slope between spring and autumn, but not in winter. These signals might originate from englacial water pressure fluctuation caused by the daily glacier meltwater cycles.

5.2. Deformation signal validation and artifacts

Our displacement data show that the monitoring system can capture displacement dynamics at a spatial and temporal resolution required to describe the processes involved (FBG system: ~ 1 με (≈ 4 μm) or below, and SAA in-place inclinometer system: ~ 0.1 mm/0.5 m). In order to investigate high-resolution FBG strain signals for the occurrence of measurement artifacts, a detailed analysis of all significant FBG strain events in the early data was conducted. It showed that: (1) most (~ 70%) of the strain signals temporally coincide with potential triggers such as rainfall or snowmelt events; (2) around 20% of the FBG strain events could be clearly detected with the lower resolution SAA inclinometer chain and for about 50% of the FBG strain events a signal close to the detectability of the SAA chain may be present; and (3) that the measured strain signals do not show systematic errors. This allows us to conclude that the majority of the measured reversible and irreversible displacement signals (as well as combinations of the two) measured with the FBG system at magnitudes between 1 μm to >200 μm reflect real displacements. An open issue when interpreting data from these high-resolution sensors is that micro-displacements within the borehole might also originate from interactions of the stiff PVC tube, the grout, and the different sensors. Longer time series will help to distinguish between such borehole artifacts and real fracture

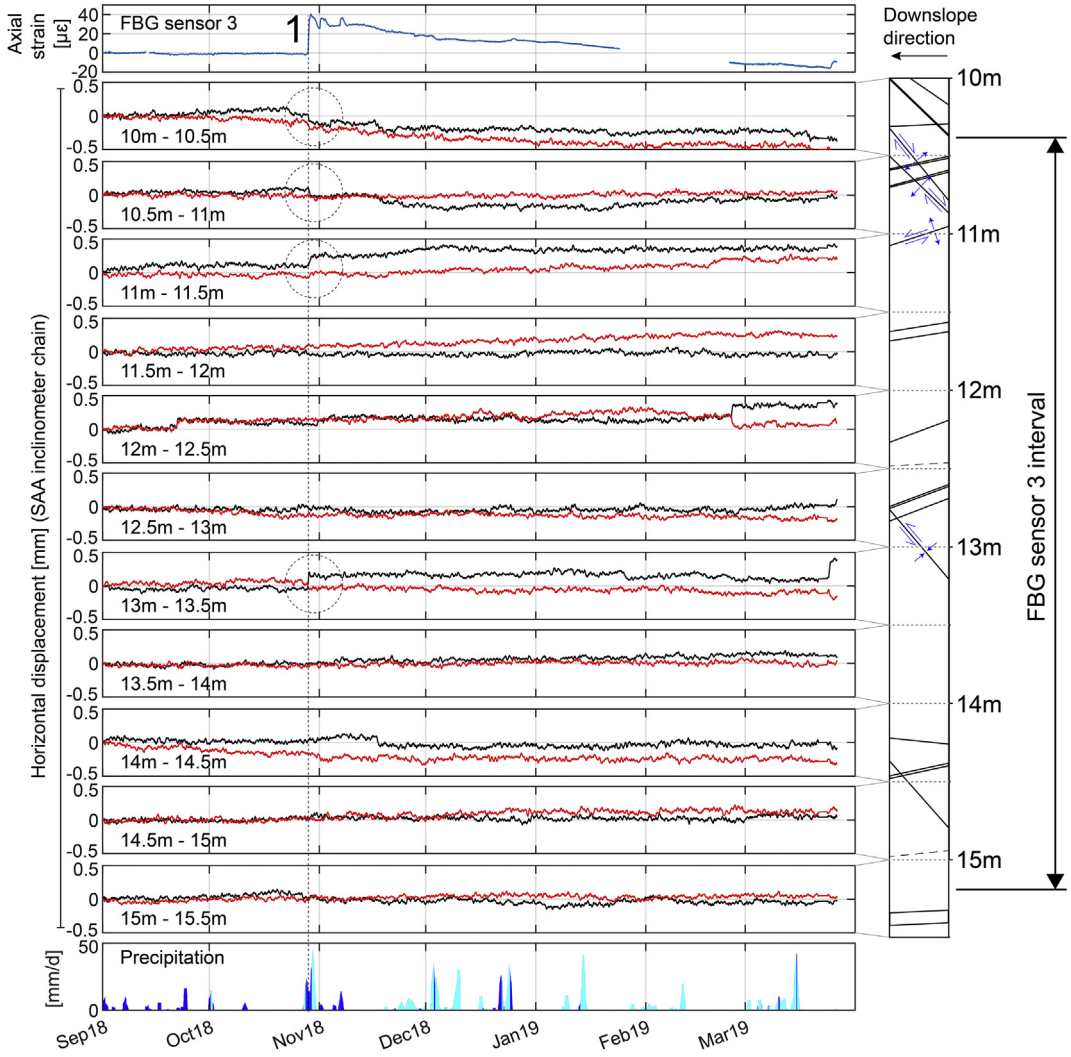

Fig. 14. Comparison of borehole axial strain measurements from FBG interval 3 (10.38–15.19 m depth) in B2 with horizontal displacements in the specific interval measured by the SAA inclinometer chain. The black lines in the SAA data show horizontal x-axis displacement in slope dip direction, whereas the red lines show horizontal y-axis displacement in slope strike direction (i.e., 90° x). In the precipitation plot, the bars show the cumulative total precipitation data (per 24 h) provided by MeteoSchweiz from the weather station "Bruchji" (Valais) located approximately 6 km away from our study site. The cyan bars indicate precipitation that presumably occurred as snow (i.e., at surface temperatures below 1 °C at our study site (cf. Jennings et al., 2018)). To the right of the monitoring data, the mapped structures from the optical televiewer log in the specific depth interval of B2 are shown in a slab core projection cutting the borehole parallel to the slope dip.

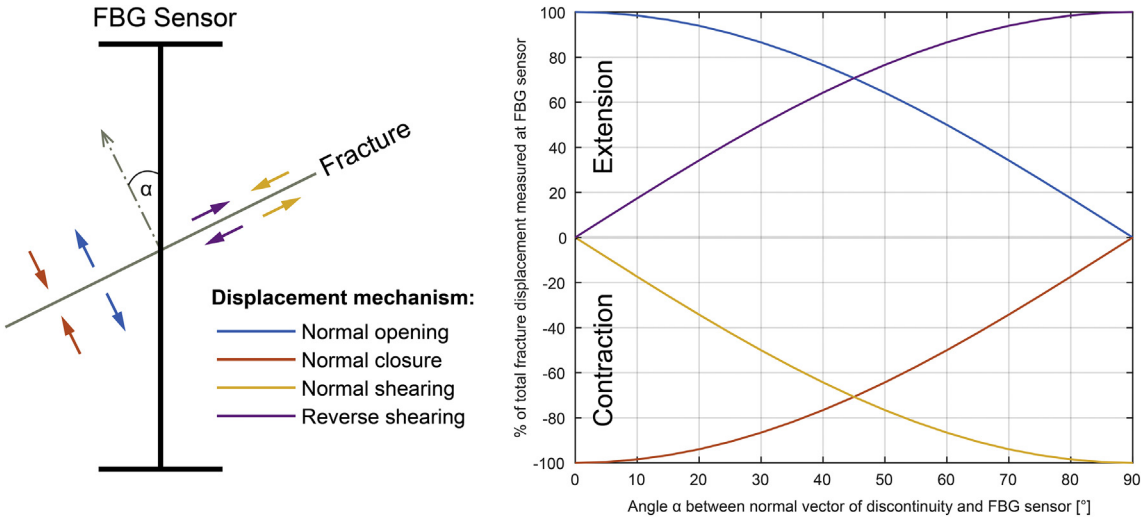

Fig. 15. Geometrical dependency of the fracture orientation relative to the FBG sensor that controls the percentage of the total fracture displacement that can be measured with the FBG sensor. Positive values mean extension and negative values contraction.

displacements. Detecting a single event with different sensor types (FBG system and SAA inclinometer) is one way to confirm that a specific strain signal is a real fracture displacement.

Horizontal displacement events measured with the SAA inclinometer can be validated by correlating them with the timing and location of strain events measured with the higher resolution FBG system. The reliability of the horizontal displacement data from the SAA in-place inclinometer was also investigated by comparing cumulative horizontal displacements over the total depth of borehole B4 with independent surface displacements measured at a nearby reflector. The two displacement measurements show similar behavior in orientation and timing, however, at different displacement magnitudes. The fact that only a part of the total horizontal surface displacement is captured in the borehole allows us to conclude that the measured total surface displacements occur down to greater depth (i.e., deeper than the borehole depth of 44 m).

5.3. Deformation characteristics and drivers

The presented data shows that reversible and irreversible displacement (or damage) events (as well as combinations of the two) often temporally coincide with potential drivers such as rainfall events, pore pressure variations due to snowmelt recharge, or extreme surface temperatures. Major pore pressure buildups due to annual snowmelt recharge in spring or recharge from extreme precipitation events cause clear deformation that can be observed at several sensors in all of the three boreholes. The displacement magnitudes measured at individual sensors during these events are in the range of a few tens of μm up to more than two mm.

Reversible deformation is observed at different timescales and displacement magnitudes. Weak daily strain fluctuations with an amplitude of about 20 μm that correlate to the diurnal pressure cycles during the summer season are measured at several FBG sensors. These strain fluctuations might be related to englacial water pressure fluctuations caused by the daily glacier meltwater cycles. At intermediate timescales, reversible deformations (of a few days to weeks) are related to pressure buildups due to recharge from heavy rainfalls or snowmelt events, and normally show magnitudes up to 100 μm at individual FBG sensors. Deformation during these events normally also includes a minor irreversible component. Surface displacement monitoring and cumulative horizontal borehole displacements further reveal reversible deformation at an annual periodicity. These deformation signals might be related to the annual pore pressure fluctuations in the slope. To date it is difficult to clearly identify the irreversible portion of the deformation related to this annual timescale because of the relatively short time series. At least a few annual cycles are necessary to clearly distinguish an irreversible component related to progressive rock mass damage.

5.4. Implications for the study of paraglacial rock slope evolution

In the framework of paraglacial rock slope evolution and in order to investigate the effect of a retreating glacier on progressive damage and stability state of adjacent rock slopes, it is of major importance to have a good knowledge of the static and dynamic boundary conditions affecting the slope. The annually acquired high-resolution aerial photos of the Great Aletsch Glacier provided by the Swiss Federal Office of Topography (swisstopo, JA100120) define the mechanical boundary condition of the ice loading and rates of ice retreat. With the borehole monitoring of pore-water pressure and temperature at variable lateral distances to the glacier, the thermal and hydraulic boundary conditions and its variability over time can be clearly captured with our monitoring system. As discussed in Sections 4.5 and 5.2 our surface and subsurface monitoring system is also able to record localized displacements at the scale of individual fractures. Future investigations will focus on the physical relationships between these displacements field and the postulated hydro-thermo-mechanical drivers.

As detailed in the introduction, rock slope failure can be the result of damage accumulation over long timescales (e.g., Riva et al., 2017). Numerical modelling results from Grämiger (2017) and Grämiger et al. (2018) show that annual loading cycles from temperature and pore pressure variations in rock slopes, superimposed on the mechanical unloading effects from glacial retreat, can induce fracture displacements on the order of 10–100 μm for thermo-mechanical processes and 100 μm per year for hydro-mechanical processes. The initial measurements from our monitoring system show that differential displacements of this magnitude are occurring along individual fractures at our study site, and often correlate with these changing boundary conditions. Thus, our initial measurements support the modelling results presented by Grämiger (2017) and Grämiger et al. (2018). However, the detailed mechanical conditions and drivers for minor fracture displacements are still unclear, especially when consider quasi-stable rock slopes and long geological time scales. As such, the strength criteria applied in the models of Grämiger (2017) will be critically reviewed in future studies of this novel data set.

The preliminary findings of this study have important implications for many fields, for example the long-term stability of underground excavations for the disposal of radioactive wastes in crystalline rocks (e.g. SKB Svensk Kärnbränslehantering AB, 2018), or the understanding of the delay between deglaciation and catastrophic rock slope failure noted by many authors (e.g., Ivy-Ochs et al., 2017). Three periods of enhanced slope failure have been noted in the Alps: 10–9 ky, 5–3 ky and 2–1 ky, which correspond to times when the climate became warmer and wetter (Zerathe et al., 2014; Ivy-Ochs et al., 2017). Our measurements support one possible mechanism that may help to explain this observation: increased rate of damage accumulation during warm and wet periods. We have directly measured damage accumulation temporally correlated with temperature and pore pressure fluctuations (e.g., Fig. 12), and we hypothesize that during warmer and wetter climate periods these would be more frequent. We postulate that the transition from a quasi-stable slope into a mature landslide is a continuous process rarely studied and discussed in literature. In Alpine crystalline rock slopes, it takes typically thousands of years to bring such a slope close to a critical stability state. Discrete damaging events, such as earthquakes, can result in rock slope failures, but many large failures in crystalline rocks occur without a clear trigger.

6. Summary and outlook

In this work, we describe the setup, performance, and data gathered from a novel high-resolution borehole monitoring system. The system is installed at a unique location in a quasi-stable rock slope along the retreating glacier tongue of the Great Aletsch Glacier (Switzerland). We have established an automatic, continuous monitoring system operating reliably in a harsh alpine environment. The monitoring system continuously records groundwater pressure, temperature variations, and fracture displacements at highest resolution in order to investigate thermo-hydro-mechanical coupled processes and their contribution to progressive rock mass damage. While in the past, the processes involved in progressive rock mass damage during the paraglacial transition were mainly investigated through numerical modelling (e.g., Grämiger, 2017), our new monitoring system provides unique and critical data supporting the analysis of paraglacial rock slope mechanics. The dataset presented here provides new information about thermal and hydraulic boundary conditions and thermo-hydro-mechanical coupled processes occurring in quasi-stable rock slopes interacting with a retreating valley glacier.

In the future, the continuously growing dataset will be quantitatively analyzed for reversible and irreversible displacement signals resulting from thermo-hydro-mechanical coupled processes, and additional data will be collected to better understand the coupling between

englacial water pressures and those in the adjacent rock slope. The integration of longer time series of displacement monitoring data and the structural information from the optical televiewer borehole logs will allow us to investigate characteristics of specific displacement events along individual fractures in 3D space in order to analyze dominant fracture modes, kinematics, and predominant driving mechanisms. This will enable us to relate the changing boundary conditions caused by glacial retreat and fatigue from daily to annual thermal and hydraulic loading cycles to progressive rock mass damage and weakening.

Declaration of competing interest

The authors declare that they have no known competing financial interests or personal relationships that could have appeared to influence the work reported in this paper.

Acknowledgements

This project is funded by the Swiss National Science Foundation (project 172492). Special thanks go to Reto Seifert for his contribution to the planning and installation of the monitoring system and for his technical support during maintenance. Also, we want to thank the numerous field assistants who supported us during the logging and instrumentation phase, helped to keep the monitoring system running during maintenance operations, and supported us with the collection of geological information in the study area. We are grateful for the inputs on FBG data analysis from Valentin Gischig and especially thank Hannes Krietsch for providing the background of the geometrical relationship between a measured FBG signal and the actual dislocation mechanism along a preexisting discontinuity used in Fig. 15.

References

Augustinus, P.C., 1995. Glacial valley cross-profile development: the influence of in situ rock stress and rock mass strength, with examples from the Southern Alps, New Zealand. Geomorphology 14 (2), 87–97. https://doi.org/10.1016/0169-555X(95)00050-X.

Ballantyne, C.K., 2002. Paraglacial geomorphology. Quat. Sci. Rev. 21 (18–19), 1935–2017. https://doi.org/10.1016/S0277-3791(02)00005-7.

Ballantyne, C.K., Sandeman, G.F., Stone, J.O., Wilson, P., 2014a. Rock-slope failure following Late Pleistocene deglaciation on tectonically stable mountainous terrain. Quat. Sci. Rev. 86, 144–157. https://doi.org/10.1016/j.quascirev.2013.12.021.

Ballantyne, C.K., Wilson, P., Gheorghiu, D., Rodes, A., 2014b. Enhanced rock-slope failure following ice-sheet deglaciation: timing and causes. Earth Surf. Process. Landf. 39 (7), 900–913. https://doi.org/10.1002/esp.3495.

Baroni, C., Martino, S., Salvatore, M.C., Mugnozza, G.S., Schiliro, L., 2014. Thermomechanical stress-strain numerical modelling of deglaciation since the Last Glacial Maximum in the Adamello Group (Rhaetian Alps, Italy). Geomorphology 226, 278–299. https://doi.org/10.1016/j.geomorph.2014.08.013.

Collins, B.D., Stock, G.M., 2016. Rockfall triggering by cyclic thermal stressing of exfoliation fractures. Nat. Geosci. 9 (5), 395–400. https://doi.org/10.1038/ngeo2686.

de Palézieux, L., Loew, S., 2019. Long-term transient groundwater pressure and deep infiltration in Alpine mountain slopes (Poschiavo Valley, Switzerland). Hydrogeol. J. 27, 2817–2834. https://doi.org/10.1007/s10040-019-02025-9.

Eberhardt, E., Stead, D., Coggan, J.S., 2004. Numerical analysis of initiation and progressive failure in natural rock slopes - the 1991 Randa rockslide. Int J Rock Mech Min 41 (1), 69–87. https://doi.org/10.1016/S1365-1609(03)00076-5.

Frukacz, M., Presl, R., Wieser, A., Favot, D., 2017. Pushing the sensitivity limits of RTS-based continuous deformation monitoring of an alpine valley. Applied Geomatics 9 (2), 81–92. https://doi.org/10.1007/s12518-017-0182-2.

Fudge, T.J., Harper, J.T., Humphrey, N.F., Pfeffer, W.T., 2005. Diurnal water-pressure fluctuations: timing and pattern of termination below Bench Glacier, Alaska, USA. Ann. Glaciol. 40, 102–106. https://doi.org/10.3189/172756405781813799.

Gischig, V.S., Moore, J.R., Evans, K.F., Amann, F., Loew, S., 2011a. Thermomechanical forcing of deep rock slope deformation: 1. Conceptual study of a simplified slope. J Geophys Res-Earth 116. https://doi.org/10.1029/2011JF002006.

Gischig, V.S., Moore, J.R., Evans, K.F., Amann, F., Loew, S., 2011b. Thermomechanical forcing of deep rock slope deformation: 2. The Randa rock slope instability. J Geophys Res-Earth 116. https://doi.org/10.1029/2011JF002007.

Gischig, V., Preisig, G., Eberhardt, E., 2016. Numerical investigation of seismically induced rock mass fatigue as a mechanism contributing to the progressive failure of deep-seated landslides. Rock Mech. Rock. Eng. 49 (6), 2457–2478. https://doi.org/10.1007/s00603-015-0821-z.

GLAMOS, 1881-2018. The Swiss Glaciers 1880–2016/17, Glaciological Reports No 1–138, Yearbooks of the Cryospheric Commission of the Swiss Academy of Sciences (SCNAT), published since 1964 by VAW/ETH Zurich. https://doi.org/10.18752/glrep_series.

Gleeson, T., Manning, A.H., 2008. Regional groundwater flow in mountainous terrain: three-dimensional simulations of topographic and hydrogeologic controls. Water Resour. Res. 44 (10). https://doi.org/10.1029/2008WR006848.

Glueer, F., 2019. Monitoring and Analysis of Interactions Between the Retreating Aletsch Glacier and Adjacent Rock Slope Instabilities. Dissertation, ETH Zurich https://doi.org/10.3929/ethz-b-000330455 (123 pp).

Glueer, F., Loew, S., Manconi, A., Aaron, J., 2019. From toppling to sliding: progressive evolution of the Moosfluh Landslide, Switzerland. Journal of Geophysical Research: Earth Surface 124 (12), 2899–2919. https://doi.org/10.1029/2019JF005019.

Glueer, F., Loew, S., Manconi, A., 2020. Paraglacial history and structure of the Moosfluh Landslide (1850-2016). Switzerland. Geomorphology 355. https://doi.org/10.1016/j.geomorph.2019.02.021.

Grämiger, L.M., 2017. Beyond Debuttressing: Thermo-Hydro-Mechanical Rock Slope Damage During Glacial Cycles. Dissertation, ETH Zurich https://doi.org/10.3929/ethz-b-000183675 (136 pp).

Grämiger, L.M., Moore, J.R., Gischig, V.S., Ivy-Ochs, S., Loew, S., 2017. Beyond debuttressing: mechanics of paraglacial rock slope damage during repeat glacial cycles. J Geophys Res-Earth 122 (4), 1004–1036. https://doi.org/10.1002/2016JF003967.

Grämiger, L.M., Moore, J.R., Gischig, V.S., Loew, S., 2018. Thermomechanical stresses drive damage of Alpine valley rock walls during repeat glacial cycles. J Geophys Res-Earth 123 (10), 2620–2646. https://doi.org/10.1029/2018JF004626.

Guglielmi, Y., Cappa, F., Binet, S., 2005. Coupling between hydrogeology and deformation of mountainous rock slopes: insights from La Clapiere area (southern Alps, France). Compt. Rendus Geosci. 337 (13), 1154–1163. https://doi.org/10.1016/j.crte.2005.04.016.

Guglielmi, Y., Cappa, F., Rutqvist, J., Tsang, C.F., Thoraval, A., 2008. Mesoscale characterization of coupled hydromechanical behavior of a fractured-porous slope in response to free water-surface movement. Int J Rock Mech Min 45 (6), 862–878. https://doi.org/10.1016/j.ijrmms.2007.09.010.

Gunzburger, Y., Merrien-Soukatchoff, V., Guglielmi, Y., 2005. Influence of daily surface temperature fluctuations on rock slope stability: case study of the Rochers de Valabres slope (France). Int J Rock Mech Min 42 (3), 331–349. https://doi.org/10.1016/j.ijrmms.2004.11.003.

Hansmann, J., Loew, S., Evans, K.F., 2012. Reversible rock-slope deformations caused by cyclic water-table fluctuations in mountain slopes of the Central Alps, Switzerland. Hydrogeol. J. 20 (1), 73–91. https://doi.org/10.1007/s10040-011-0801-7.

Harper, J.T., Humphrey, N.F., Pfeffer, W.T., Fudge, T., O'Neel, S., 2005. Evolution of subglacial water pressure along a glacier's length. Ann. Glaciol. 40, 31–36. https://doi.org/10.3189/172756405781813573.

Holzhauser, H., Magny, M., Zumbuhl, H.J., 2005. Glacier and lake-level variations in west-central Europe over the last 3500 years. Holocene 15 (6), 789–801. https://doi.org/10.1191/0959683605hl853ra.

Hubbard, B.P., Sharp, M.J., Willis, I.C., Nielsen, M.K., Smart, C.C., 1995. Borehole water-level variations and the structure of the subglacial hydrological system of Haut Glacier Darolla, Valais, Switzerland. J. Glaciol. 41 (139), 572–583. https://doi.org/10.3189/S0022143000034894.

Ivy-Ochs, S., Kerschner, H., Reuther, A., Preusser, F., Heine, K., Maisch, M., Kubik, P.W., Schlüchter, C., 2008. Chronology of the last glacial cycle in the European Alps. J. Quat. Sci. 23 (6–7), 559–573. https://doi.org/10.1002/jqs.1202.

Ivy-Ochs, S., Poschinger, A.V., Synal, H.A., Maisch, M., 2009. Surface exposure dating of the Flims landslide, Graubunden, Switzerland. Geomorphology 103 (1), 104–112. https://doi.org/10.1016/j.geomorph.2007.10.024.

Ivy-Ochs, S., Martin, S., Campedel, P., Hippe, K., Alfimov, V., Vockenhuber, C., Andreotti, E., Carugati, G., Pasqual, D., Rigo, M., Vigano, A., 2017. Geomorphology and age of the Marocche di Dro rock avalanches (Trentino, Italy). Quat. Sci. Rev. 169, 188–205. https://doi.org/10.1016/j.quascirev.2017.05.014.

Jennings, K.S., Winchell, T.S., Livneh, B., Molotch, N.P., 2018. Spatial variation of the rain–snow temperature threshold across the Northern Hemisphere. Nat. Commun. 9 (1), 1148. https://doi.org/10.1038/s41467-018-03629-7.

Kelly, M.A., Kubik, P.W., Von Blanckenburg, F., Schlüchter, C., 2004. Surface exposure dating of the Great Aletsch Glacier Egesen moraine system, western Swiss Alps, using the cosmogenic nuclide 10Be. J. Quat. Sci. 19 (5), 431–441. https://doi.org/10.1002/jqs.854.

Kos, A., Amann, F., Strozzi, T., Delaloye, R., von Ruette, J., Springman, S., 2016. Contemporary glacier retreat triggers a rapid landslide response, Great Aletsch Glacier. Switzerland. Geophys. Res. Lett. 43 (24), 12466–12474. https://doi.org/10.1002/2016GL071708.

Krietsch, H., 2019. Hydro-mechanical responses of a fractured rock mass during decameter-scale hydraulic stimulation experiments. Dissertation, ETH Zurich. https://doi.org/10.3929/ethz-b-000372209.

Lappegard, G., Kohler, J., Jackson, M., Hagen, J.O., 2006. Characteristics of subglacial drainage systems deduced from load-cell measurements. J. Glaciol. 52 (176), 137–148. https://doi.org/10.3189/172756506781828908.

Limpach, P., Geiger, A., Raetzo, H., 2016. GNSS for Deformation and Geohazard Monitoring in the Swiss Alps, 3rd Joint International Symposium on Deformation Monitoring (JISDM 2016). International Federation of Surveyors, Vienna, Austria http://hdl.handle.net/20.500.11850/126642.

Loew, S., Ebneter, F., Bremen, R., Herfort, M., Lützenkirchen, V., Matousek, F., 2007. Annual opening and closure of Alpine valleys. Felsbau: Rock and Soil Engineering 25 (5), 60–65.

Loew, S., Gischig, V., Glueer, F., Seifert, R., Moore, J., 2017. Multidisciplinary monitoring of progressive failure processes in brittle rock slopes. In: Feng, X.-T. (Ed.), Rock Mechanics and Engineering. CRC Press, pp. 629–662.

McColl, S.T., 2012. Paraglacial rock-slope stability. Geomorphology 153-154, 1–16. https://doi.org/10.1016/j.geomorph.2012.02.015.
McColl, S.T., Davies, T.R.H., 2013. Large ice-contact slope movements: glacial buttressing, deformation and erosion. Earth Surf. Process. Landf. 38 (10), 1102–1115. https://doi.org/10.1002/esp.3346.
McColl, S.T., Draebing, D., 2019. Rock slope instability in the proglacial zone: state of the art. In: Heckmann, T., Morche, D. (Eds.), Geomorphology of Proglacial Systems. Springer International Publishing, Cham, pp. 119–140.
McColl, S.T., Davies, T.R.H., McSaveney, M.J., 2010. Glacier retreat and rock-slope stability: debunking debuttressing. In: Williams, A.L., Pinches, G.M., Chin, C.Y., McMorran, T.J., Massey, C.I. (Eds.), 11th Congress of the International Association for Engineering Geology and the Environment, pp. 467–474 Boca Raton, FL, United States: CRC Press, Auckland, Aotearoa.
Morey, W.W., Meltz, G., Glenn, W.H., 1990. Fiber optic Bragg grating sensors, fiber optic and laser sensors VII. SPIE, Boston, United States. https://doi.org/10.1117/12.963022.
Pollack, H.N., 1993. Climate-change inferred from borehole temperatures. Glob. Planet. Chang. 7 (1–3), 173–179. https://doi.org/10.1016/0921-8181(93)90048-S.
Pollack, H.N., Huang, S.P., 2000. Climate reconstruction from subsurface temperatures. Annu Rev Earth Pl Sc 28, 339–365. https://doi.org/10.1146/annurev.earth.28.1.339.
Prager, C., Zangerl, C., Patzelt, G., Brandner, R., 2008. Age distribution of fossil landslides in the Tyrol (Austria) and its surrounding areas. Nat Hazard Earth Sys 8 (2), 377–407. https://doi.org/10.5194/nhess-8-377-2008.
Preisig, G., Eberhardt, E., Smithyman, M., Preh, A., Bonzanigo, L., 2016. Hydromechanical rock mass fatigue in deep-seated landslides accompanying seasonal variations in pore pressures. Rock Mech. Rock. Eng. 49 (6), 2333–2351. https://doi.org/10.1007/s00603-016-0912-5.
Riva, F., Agliardi, F., Amitrano, D., Crosta Giovanni, B., 2017. Damage-based time-dependent modeling of paraglacial to postglacial progressive failure of large rock slopes. Journal of Geophysical Research: Earth Surface 123 (1), 124–141. https://doi.org/10.1002/2017JF004423.
Rouyet, L., Kristensen, L., Derron, M.H., Michoud, C., Blikra, L.H., Jaboyedoff, M., Lauknes, T.R., 2017. Evidence of rock slope breathing using ground-based InSAR. Geomorphology 289, 152–169. https://doi.org/10.1016/j.geomorph.2016.07.005.
Rutqvist, J., Stephansson, O., 2003. The role of hydromechanical coupling in fractured rock engineering. Hydrogeol. J. 11 (1), 7–40. https://doi.org/10.1007/s10040-002-0241-5.
Rybach, L., Pfister, M., 1994. Temperature predictions and predictive temperatures in deep tunnels. Rock Mech. Rock. Eng. 27 (2), 77–88. https://doi.org/10.1007/BF01020206.
Schindelwig, I., Akçar, N., Kubik, P.W., Schlüchter, C., 2012. Lateglacial and early Holocene dynamics of adjacent valley glaciers in the Western Swiss Alps. J. Quat. Sci. 27 (1), 114–124. https://doi.org/10.1002/jqs.1523.
Singhal, B.B.S., Gupta, R.P., 2010. Applied Hydrogeology of Fractured Rocks. Springer, Dordrecht https://doi.org/10.1007/978-90-481-8799-7_2.
SKB Svensk Kärnbränslehantering AB, 2018. Long-term safety for the final repository for spent nuclear fuel at Forsmark. Main Report of the SR-Site Project Volume 1, p. 276 ISSN 1404-0344, Report SKB TR-11-01.
Smith, S.W., 1997. The Scientist and Engineer's Guide to Digital Signal Processing. California Technical Publishing, San Diego, CA, Digital signal processing.
Steck, A., 2011. 1269 Aletschgletscher mit Teil von 1249 Finsteraarhorn. Geolog. Atlas der Schweiz 1, 25000.
Strozzi, T., Delaloye, R., Kaab, A., Ambrosi, C., Perruchoud, E., Wegmuller, U., 2010. Combined observations of rock mass movements using satellite SAR interferometry, differential GPS, airborne digital photogrammetry, and airborne photography interpretation. J Geophys Res-Earth 115 (F1). https://doi.org/10.1029/2009JF001311.
Wegmann, M., Gudmundsson, G.H., Haeberli, W., 1998. Permafrost changes in rock walls and the retreat of alpine glaciers: a thermal modelling approach. Permafrost Periglac 9 (1), 23–33. https://doi.org/10.1002/(SICI)1099-1530(199801/03)9:1<23::AID-PPP274>3.0.CO;2-Y.
Zangerl, C., Eberhardt, E., Loew, S., 2003. Ground settlements above tunnels in fractured crystalline rock: numerical analysis of coupled hydromechanical mechanisms. Hydrogeol. J. 11 (1), 162–173. https://doi.org/10.1007/s10040-002-0234-4.
Zerathe, S., Lebourg, T., Braucher, R., Bourlès, D., 2014. Mid-Holocene cluster of large-scale landslides revealed in the Southwestern Alps by 36Cl dating. Insight on an Alpine-scale landslide activity. Quat. Sci. Rev. 90, 106–127. https://doi.org/10.1016/j.quascirev.2014.02.015.
Zhu, H.H., Shi, B., Zhang, C.C., 2017. FBG-based monitoring of geohazards: current status and trends. Sensors 17 (3). https://doi.org/10.3390/s17030452.